Quantification of CH_4 emissions from waste disposal sites near the city of Madrid using ground- and space-based observations of COCCON, TROPOMI and IASI

Qiansi Tu[1], Frank Hase[1], Matthias Schneider[1], Omaira García[2], Thomas Blumenstock[1], Tobias Borsdorff[3], Matthias Frey[1,a], Farahnaz Khosrawi[1], Alba Lorente[3], Carlos Alberti[1], Juan J. Bustos[2], André Butz[4], Virgilio Carreño[2], Emilio Cuevas[2], Roger Curcoll[5,b], Christopher J. Diekmann[1], Darko Dubravica[1], Benjamin Ertl[1,6], Carme Estruch[5], Sergio Fabián León-Luis[2], Carlos Marrero[2], Josep-Anton Morgui[5], Ramón Ramos[2], Christian Scharun[1], Carsten Schneider[4], Eliezer Sepúlveda[2], Carlos Toledano[7], Carlos Torres[2]

[1] Karlsruhe Institute of Technology (KIT), Institute of Meteorology and Climate Research (IMK-ASF), Karlsruhe, Germany
[a] now at National Institute for Environmental Studies, Tsukuba, Japan
[2] Izaña Atmospheric Research Centre (IARC), Meteorological State Agency of Spain (AEMet), Tenerife, Spain
[3] SRON Netherlands Institute for Space Research, Utrecht, the Netherlands
[4] Institut für Umweltphysik, Heidelberg University (UH), Germany
[5] Institut de Ciència i Tecnologia Ambientals (ICTA) - Autonomous University of Barcelona, Spain
[b] now at Institute of Energy Technologies, Polytechnic University of Catalonia, Barcelona, Spain
[6] Karlsruhe Institute of Technology, Steinbuch Centre for Computing (SCC), Karlsruhe, Germany
[7] Group of Atmospheric Optics, University of Valladolid, Spain

Correspondence to: Qiansi Tu (qiansi.tu@kit.edu)

Abstract. The objective of this study is to derive methane (CH_4) emissions from three landfills, which are found to be the most significant CH_4 sources in the metropolitan area of Madrid in Spain. We derive CH_4 emissions from the CH_4 enhancements observed by space-borne and ground-based instruments. We apply satellite-based measurements from the TROPOspheric Monitoring Instrument (TROPOMI) and the Infrared Atmospheric Sounding Interferometer (IASI) together with measurements from the ground-based COllaborative Carbon Column Observing Network (COCCON) instruments.

In 2018, a two-week field campaign for measuring the atmospheric concentrations of greenhouse gases was performed in Madrid in the framework of Monitoring greenhousE Gas EmIssions of Madrid city (MEGEI-MAD) project. Five COCCON instruments were deployed at different locations around the Madrid city center enabling the observation of total column-averaged CH_4 mixing ratios (XCH_4). Considering the prevalent wind regimes, we calculate the wind-assigned XCH_4 anomalies for two opposite wind directions. Pronounced bipolar plumes are found, when applying the method to NO_2, which implies that our method of wind-assigned anomaly is suitable to estimate enhancements of trace gases at urban level from satellite-based measurements. For quantifying the CH_4 emissions, the wind-assigned plume method is applied to the TROPOMI XCH_4 and to the lower tropospheric CH_4/dry air column ratio ($TXCH_4$) of the combined TROPOMI+IASI product.

As CH_4 emission strength we estimate $7.4\times10^{25} \pm 6.4\times10^{24}$ molec s^{-1} from the TROPOMI XCH_4 data and $7.1\times10^{25} \pm 1.0\times10^{25}$ molec s^{-1} from the TROPOMI+IASI merged $TXCH_4$ data. We use COCCON observations to estimate the local source strength

as an independent method. COCCON observations indicate a weaker CH_4 emission strength of 3.7×10^{25} molec s^{-1} from a local source (the Valdemingómez waste plant) based on observations from a single day. That this strength is lower than the one derived from the satellite observations is a plausible result. This is because the analysis of the satellite data refers to a larger area, covering further emission sources in the study region, whereas the signal observed by COCCON is generated by a nearby local source. All emission rates estimated from the different observations are significantly larger than the emission rates provided via the official Spanish Register of Emissions and Pollutant Sources.

1 Introduction

Methane (CH_4) is the second most important anthropogenic greenhouse gas (GHG) after carbon dioxide (CO_2) and contributes about 23.4% to the radiative forcing by long-lived GHGs in the atmosphere (Etminan et al., 2016). The amount of atmospheric CH_4 has increased 260% with respect to pre-industrial levels, reaching 1880 ppb in 2019 (World Meteorological Organization, 2020). The global atmospheric CH_4 emissions are ~~to~~ approximately 40% caused by natural sources (e.g. wetlands and termites) and by about 60% from anthropogenic sources (Saunois et al., 2020). The anthropogenic sources of CH_4 mainly originate from production and burning of fossil fuels, ruminant animals, agriculture and waste management (Bousquet et al., 2006; Chynoweth et al., 2001; Kirschke et al., 2013; Saunois et al., 2020). The waste management sector accounts for 21.5% of the total anthropogenic CH_4 emissions (Crippa et al., 2019), in which ~~while~~ ~44% of emissions are from landfills. The global uncertainty share of landfills is about ~~(~~ ~~~~~ 55% ~~uncertainty)~~ (Solazzo et al., 2021). The metropolitan cities are continuously growing due to population movements, industries, etc., and thus, more and more cities incorporate landfills (and other potential CH_4 sources) into their limits and influential areas, making landfills become one of the main CH_4 sources. Since CH_4 emissions from landfills can vary over several orders of magnitude due to different factors, e.g. the texture and thickness of cover soils, seasonal climate, they become complex sources (Cambaliza et al., 2015). Therefore, the quantification of CH_4 emission from landfills using ~~space~~ space-borne and ground-based observations is of importance for future climate emission scenarios and for monitoring changes in emissions.

Many studies have demonstrated the capabilities of satellite observations to estimate CH_4 emissions e.g. from oil and gas sector, including accidental leakages (e.g. Pandey et al., 2019; Varon et al., 2019; Gouw et al., 2020; Schneising et al., 2020) and from coal mining (Varon et al., 2020). ~~Here, we use satellite observations together with ground-based measurements from portable Fourier Transform Infrared (FTIR) spectrometers to derive CH_4 emissions from landfills in a metropolitan area.~~
Launched in October 2017, the TROPOspheric Measuring Instrument (TROPOMI) on board the Copernicus Sentinel-5 Precursor satellite provides complete daily global coverage of CH_4 with an unprecedented resolution. Compared to previous satellite instruments, TROPOMI is able to capture CH_4 enhancements due to emissions on fine scales and to detect large point sources (Varon et al., 2019; Gouw et al., 2020; Schneising et al., 2020). Satellite retrievals using thermal infrared nadir spectra as observed by IASI (Infrared Atmospheric Sounding Interferometer) or TES (Tropospheric Emission Spectrometer) are especially sensitive to CH_4 concentrations between the middle troposphere and the stratosphere (e.g. Siddans et al., 2017;

García et al., 2018; De Wachter et al, 2017; Kulawik et al., 2021; Schneider et al., 2021a). Schneider et al. (2021a) developed an a posteriori method for combining the TROPOMI and IASI products to detect tropospheric CH_4 which has a positive bias of ~1% with respect to the reference data.

The Total Carbon Column Observing Network (TCCON) network, a network of high-resolution FTIR spectrometers (Washenfelder et al., 2006), has been designed to provide accurate and long-lasting time series of column-averaged dry-air molar fractions of GHGs and other atmospheric constituents (Wunch et al., 2011). Recently, TCCON GHG observations have been extended by the COllaborative Carbon Column Observing Network (COCCON, Frey et al., 2019), which is a research infrastructure using well-calibrated low-resolution FTIR spectrometers (Bruker EM27/SUN, Gisi et al, 2012) and a common data analysis scheme. Due to the ruggedness of the portable devices used and simple operability, COCCON is well suited for implementing arrays of spectrometers into metropolitan areas for the quantification of local GHG sources (Hase et al., 2015; Luther et al., 2019; Vogel et al., 2019; Dietrich et al., 2021).

Madrid, Spain is one of the biggest cities in Europe and has almost 3.3 million inhabitants with an area population of approximately 6.5 million. Thus, the wastes are one of the main CH4 emission sources. To measure atmospheric concentrations of GHGs in this urban environment, a two-week campaign was carried out in the framework of the Monitoring greenhousE Gas EmIssions of Madrid (MEGEI-MAD) project (García et al., 2019) from September 24 to October 7, 2018 in Madrid.

In this study we analyze nearly three years of TROPOMI total column-average dry-air molar fraction of CH_4 (XCH_4) measurements, TROPOMI+IASI TXCH4 measurements together with COCCON spectrometer observations made during the MEGEI-MAD campaign in the framework of the Monitoring greenhousE Gas EmIssions of Madrid (MEGEI-MAD) project (García et al., 2019), in an attempt to quantify the CH_4 emissions from major emission sources – namely three landfills in Madrid, the most important metropolitan area of Spain. In Section 2 our methodology is described, which is as follows: we calculate the difference of the satellite data maps for two opposite wind regimes (we refer to the resulting signals as wind-assigned anomalies). A simple plume model is then applied to predict the wind-assigned anomalies for a chosen position and strength of a source. The results of our study are presented and discussed in Section 3 and the conclusions from these results are given in Section 4.

2 Method

2.1 Ground-based and space-borne instrumentations

2.1.1 COCCON XCH_4 data set

The Bruker EM27/SUN is a robust and portable FTIR spectrometer, operating at a medium spectral resolution of 0.5 cm^{-1}. The EM27/SUN FTIR spectrometer has been developed by the Karlsruhe Institute of Technology (KIT) in cooperation with Bruker Optics GmbH for measuring GHG concentrations (Gisi et al., 2012; Hase et al., 2016). An InGaAs (Indium-Gallium-Arsenide) photodetector is used as the primary detector, covering a spectral range of 5500 – 11000 cm^{-1}. A decoupling mirror reflects

40% of the incoming converging beam to an extended InGaAs photodetector element, covering the spectral range of 4000 – 5500 cm^{-1} for simultaneous carbon monoxide (CO) observations. The recording time, for a typical measurement consisting of five forward and five backward scans, is about 58 seconds in total.

Several successful field campaigns and long-term deployments have demonstrated that the Bruker EM27/SUN FTIR spectrometer is an excellent instrument with good quality, robustness and reliability and its performance offers the potential to support TCCON (Frey et al., 2015 and 2019; Klappenbach et al., 2015; Chen et al., 2016; Butz et al., 2017; Sha et al., 2019; Jacobs et al., 2020; Tu et al., 2020a and 2020b; Dietrich et al., 2021). The Bruker EM27/SUN spectrometers have become commercially available from April 2014 onwards and currently about 70 spectrometers are operated by different working groups in Germany, France, Spain, Finland, Romania, USA, Canada, UK, India, Korea, Botswana, Japan, China, Mexico, Brazil, Australia and New Zealand. The development of the COCCON (https://www.imk-asf.kit.edu/english/COCCON.php) became possible by continued European Space Agency (ESA) support. COCCON intends to become a supporting infrastructure for GHG measurements based on common standards and data analysis procedures for the EM27/SUN (Frey et al., 2019).

All the Bruker EM27/SUN spectrometers used in the MEGEI-MAD project were operated in accordance with COCCON requirements. The resulting XCH_4 data used in this work were generated by the central facility operated by KIT for demonstrating a centralized data retrieval for the COCCON network. For these reasons, we refer to the Bruker EM27/SUN spectrometers as COCCON spectrometers in the following. The COCCON XCH_4 data product is derived from the co-observed total column amounts of CH_4 and oxygen (O_2), and the assumed dry-air molar fraction of O_2 (0.2095) (Wunch et al., 2015).

$$XCH_4 = \frac{column_{CH_4}}{column_{O_2}} \times 0.2095 \quad \textbf{Eq. 1}$$

2.1.2 TROPOMI XCH_4 data set

The TROPOMI data processing deploys the RemoTeC algorithm (Butz et al., 2009, 2011; Hasekamp and Butz, 2008) to retrieve XCH_4 from TROPOMI measurements of sunlight backscattered by the Earth's surface and atmosphere in the near-infrared (NIR) and shortwave-infrared (SWIR) spectral bands (Hu et al., 2016, 2018; Hasekamp et al., 2019; Landgraf et al., 2019). This algorithm has been extensively used to derive CH_4 and CO_2 from GOSAT (Butz et al, 2011; Guerlet et al., 2013). The TROPOMI XCH_4 is calculated from the CH_4 vertical sub-columns x_i and the dry-air column obtained from the surface pressure from European Centre for Medium-Range Weather Forecasts (ECMWF), and the altitude from the Shuttle Radar Topography Mission (SRTM) (Farr et al., 2007) digital elevation map with a resolution of 15 arcsec (Lorente et al., 2021):

$$XCH_4 = \sum_{i=0}^{n} \frac{x_i}{column_{dryair}} \quad \textbf{Eq. 2}$$

This study uses the TROPOMI data set of XCH_4 from Lorente et al., (2021), for which an updated retrieval algorithm was implemented to obtain a data set with less scatter. This updated XCH_4 has been demonstrated to be in good agreement with TCCON (-3.4 ± 5.6 ppb) and GOSAT (-10.3 ± 16.8 ppb), with a bias and precision below 1%. Here the TROPOMI XCH_4 between April 30, 2018 and December 30, 2020 within the rectangular area of 39.5°N – 41.5°N and 4.5°W – 3.0°W (125 km

× 220 km) over Madrid is analyzed. In addition, we apply a strict quality control to TROPOMI XCH_4 (quality value q = 1.0) to exclude data of questionable quality and to assure data under clear-sky and low-cloud atmospheric conditions (Lorente et al., 2021).

2.1.3 IASI CH_4 data and its synergetic combination with TROPOMI data

Satellite retrievals using thermal infrared nadir spectra as observed by IASI (Infrared Atmospheric Sounding Interferometer) or TES (Tropospheric Emission Spectrometer) are especially sensitive to CH_4 concentrations between the middle troposphere and the stratosphere (e.g. Siddans et al., 2017; García et al., 2018; De Wachter et al, 2017; Kulawik et al., 2021; Schneider et al., 2021a). The IASI sensors are currently orbiting aboard of three Metop (Meteorological operational) satellites and offers global coverage twice daily with high horizontal resolution (ground pixel diameter at nadir is 12 km). The IASI CH_4 products have a particular good quality and sensitivity as documented in validation studies (e.g. Siddans et al., 2017; De Wachter et al., 2017; García et al., 2018; Schneider et al., 2021a).

Here we use the IASI CH_4 product as generated by the latest MUSICA IASI processor version (Schneider et al., 2021b). Combing these IASI profile data with the TROPOMI total column data causes strong synergies. Schneider et al. (2021a) developed an a posteriori method for such a synergetic combination and documented the possibility to detect tropospheric partial column-averaged dry-air molar fractions of CH_4 ($TXCH_4$) independently from the upper tropospheric/stratospheric dry-air molar fractions of CH_4 ($UTSXCH_4$). This is not possible by either the TROPOMI or IASI product individually. In this study we use a tropospheric product averaged from ground to 7 km a.s.l., and an upper tropospheric/stratospheric product averaged from 7 to 20 km a.s.l.

2.2 COCCON Madrid campaign

Madrid has almost 3.3 million inhabitants with a metropolitan area population of approximately 6.5 million. Madrid is located on the Meseta Central and 60 km south of the Guadarrama mountains with a considerable altitude difference across the city, ranging from 570 to 700 m a.s.l.

This work was made in the framework of the MEGEI-MAD project (García et al., 2019), which aimed to measure atmospheric concentrations of GHGs in an urban environment combing FTIR instruments and ground-level analyzers. Another objective of MEGEI-MAD was to analyze the possible use of portable COCCON instruments to shape an operational network for Madrid in the future. The MEGEI-MAD project was initiated by the Izaña Atmospheric Research Center (AEMet), in cooperation with two German research groups – the Karlsruhe Institute of Technology and the University of Heidelberg, and two Spanish research groups – the Autonomous University of Barcelona and the University of Valladolid.

Within MEGEI-MAD, a two-week field campaign was carried out from September 24 to October 7, 2018 in Madrid, where five COCCON instruments were located at five different places circling the metropolitan area (see Figure 1). Table 1Table 1 summaries the coordinates, altitudes of the COCCON locations and auxiliary meteorological data collected for data analysis of the observations. The locations have been chosen by considering the prevailing winds and the emission sources of CO_2 and CH_4, as well as other technical and logistic criteria (García et al., 2019; García et al., 2021, in preparation).

Table 1: Locations of the five COCCON instruments and meteorological records for the MEGEI-MAD field campaign during September 24 – October 7, 2018.

Station	EM27/SUN	Latitude (°N)	Longitude (°W)	Altitude (m a.s.l.)	Meteorological Records
Tres Olivos	KIT SN53	40.499	3.689	736	Datalogger from AEMet Barajas Airport
Barajas	AEMet SN85	40.465	3.581	637	Barajas Airport
Jose Echegaray	DLR SN69	40.379	3.613	633	Datalogger from DLR Cuatro Vientos Airport
Cuatro Vientos	KIT SN52	40.368	3.780	703	Cuatro Vientos Airport
AEMeT	KIT SN81	40.452	3.724	685	AEMeT Headquarter

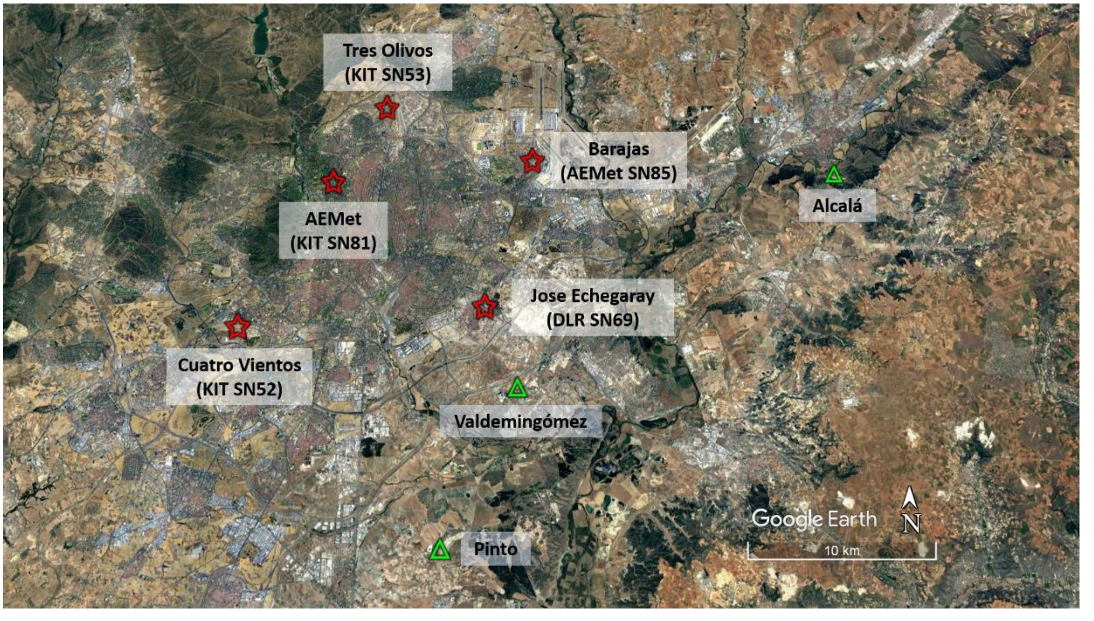

Figure 1: Locations of the five COCCON instruments used in the Madrid field campaign during September 24 – October 7, 2018, represented with red stars and locations of three waste treatment and disposal plants, represented with the green triangles.

2.3 Emission strength calculation using a simple plume model

The daily plume is modelled as a function of wind direction and wind speed. The schematic dispersion model for describing emissions assumes an expanding cone-shaped plume with the tip at the plume source at location $(0,0)$. The plume cone has an opening angle of size α and any grid cell within the cone is affected by the emission (see Figure 2). The angle α is a technical parameter to schematically describe a spreading of the plume and is empirically adjusted to a value of 60º. Different opening angles are modelled and presented in Figure A- 1. The modelled plume has the most similar shape compared to the TROPOMI measured NO_2 plume (see Section 3.3) when α>=60º. If the grid cell (x, y) locates inside the cone, the column enhancement for this cell can be calculated by:

$$\Delta colunm_{(x,y)} = \frac{\varepsilon}{v \cdot d_{(x,y)} \cdot \alpha} \quad \textbf{Eq. 3}$$

where ε is the emission strength at the source point in molec s^{-1}, v is the wind speed in m s^{-1}, d is the distance between the downwind point and the source, α is the opening angle of the plume in rad (here assumed to be 60°).

The distance from a general grid cell (x, y) from the source is:

$$d(x, y) = \sqrt{x^2 + y^2} \quad \textbf{Eq. 4}$$

The enhanced dry-air volume mixing ratio for target species (ΔXVMR) at the center of the grid cell (x, y) can then be calculated by dividing the column enhancement by the total column of dry air ($column_{dryair}$):

$$\Delta XVMR = \frac{\Delta colunm_{(x,y)}}{column_{dryair}} \quad \textbf{Eq. 5}$$

The $column_{dryair}$ is computed from the surface pressure:

$$column_{dryair} = \frac{P_S}{m_{dryair} \cdot g(\varphi)} - \frac{m_{H_2O}}{m_{dryair}} \cdot column_{H_2O} \quad \textbf{Eq. 6}$$

where P_s is the surface pressure, m_{dryair} and m_{H_2O} are the molecular masses of dry air ($\sim$28.96 g $\cdot$ mol^{-1}) and water vapor ($\sim$18 g $\cdot$ mol^{-1}), respectively. $column_{dryair}$ and $column_{H_2O}$ are the total column amount of dry air and water vapor, and $g(\varphi)$ is the latitude-dependent surface acceleration due to gravity.

In this study, each individual landfill is considered as an individual point source. The daily plumes from the individual landfills are super-positioned to have a total daily plume. The averaged enhancement of XVMR (plume) over the study area is computed for the selected wind sector. The plume for the opposite wind regime is also constructed in the same manner. The differences between these two data sets are therefore the wind-assigned anomalies (see Sect. 3.3). By fitting the modelled wind-assigned anomalies to the anomalies as observed by the satellite, we can estimate the actual emission strength (see Sect. B.2). Note that the applied calculation scheme would also be extendible to areal sources by superimposing such calculations using different locations of the origin.

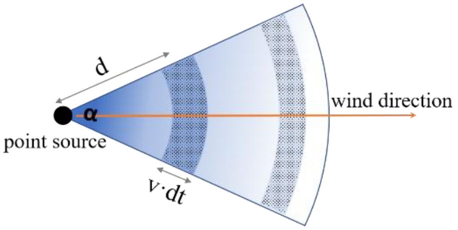

Figure 2: Sketch of the simple plume model used to explain the CH_4 emission estimation method. The methane at the point source is distributed along the wind direction (wind speed: v) in the cone-shaped area with an opening angle of α. The point source emits the methane at an emission rate of ε. We assumed the methane molecules are evenly distributed in the dotted area A, and the distance from area A to the point source is d. Therefore, the emitted methane in dt time period equals to the amount of methane in the area A. It yields the equation $\varepsilon \times dt \approx \Delta column \times \frac{\alpha}{\pi} \times \pi \times d \times v \times dt$.

3 Results and discussion

3.1 Intercomparison of TROPOMI and COCCON XCH_4 measurements

To detect whether TROPOMI is capable of measuring XCH_4 precisely in the Madrid area, we perform intercomparison between TROPOMI and COCCON XCH_4 measurements. Figure 3 shows the correlation between COCCON and TROPOMI measurements. The mean value of TROPOMI XCH_4 is calculated by collecting observations within a radius of 5 km around each COCCON station. The coincident COCCON mean XCH_4 is calculated from the measurements within 30 minutes before or after the TROPOMI overpass. The distance between two stations ranges between 6 km and 14.2 km. The TROPOMI data within a circle with a larger radius might cover the information from other nearby stations, which brings an error in the correlation between the coincident data. Therefore, we choose a collection circle with a radius of 5 km for TROPOMI. The coincident data at each station show generally good agreement. Note that there are 1 to 2 TROPOMI measurements located within a circle of 5 km radius around each station. The mean bias in XCH_4 between TROPOMI and COCCON is 2.7 ± 13.2 ppb, which is below the absolute bias between TROPOMI and TCCON (3.4 ± 5.6 ppb, Lorente et al., 2021). The higher scatter of the validation with COCCON reflects the shorter temporal and spatial collocation, but the agreement indicates that TROPOMI data have good quality and a low bias.

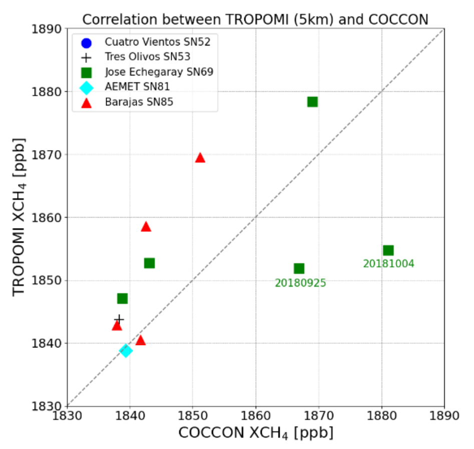

Figure 3: Correlation plot between TROPOMI observations collected within 5 km radius around each COCCON station and coincident COCCON measurements (30 minutes before and after the TROPOMI overpass) at five stations in 2018.

The coincident data on September 25, 2018 and October 4, 2018 show large biases at Jose Echegaray station where the SN69 COCCON instrument is located. Due to its coarser spatial resolution, the TROPOMI XCH_4 observations do not capture the local enhancements detected by the COCCON instrument in the vicinity of the source. Figure 4~~Figure 4~~ illustrates the two exemplary days of the time series of COCCON SN69 and coincident TROPOMI observations. Obvious enhancements are observed at around 13:00 UTC by the COCCON instrument in the downwind site on September 25 and at around 12:30 on October 4, 2018 (see Figure A- 2 for the other days). Note that the XCH_4 enhancements can also be observed by the instruments at other stations when the CH_4 plume passes over Madrid. We only discuss the two representative days with obvious enhancements here, as we focus on the specific source near the Jose Echegaray station. The Valdemingómez and Pinto waste plants are located nearby with a distance of 4.5 km and 12 km, respectively. These five COCCON stations can serve as an independent source of information for constraining the wind speed. For example, the distance between the Jose Echegaray and Barajas is about 10 km. The highest anomalies of XCH_4 arrived around 1.5 hours later at Barajas station than it appeared at the Jose Echegaray station on 25 September 2018, which indicates an averaged wind speed of 1.8 m/s. This value fits well with~~to~~ the wind velocity observed at the Cuatro Vientos Airport.

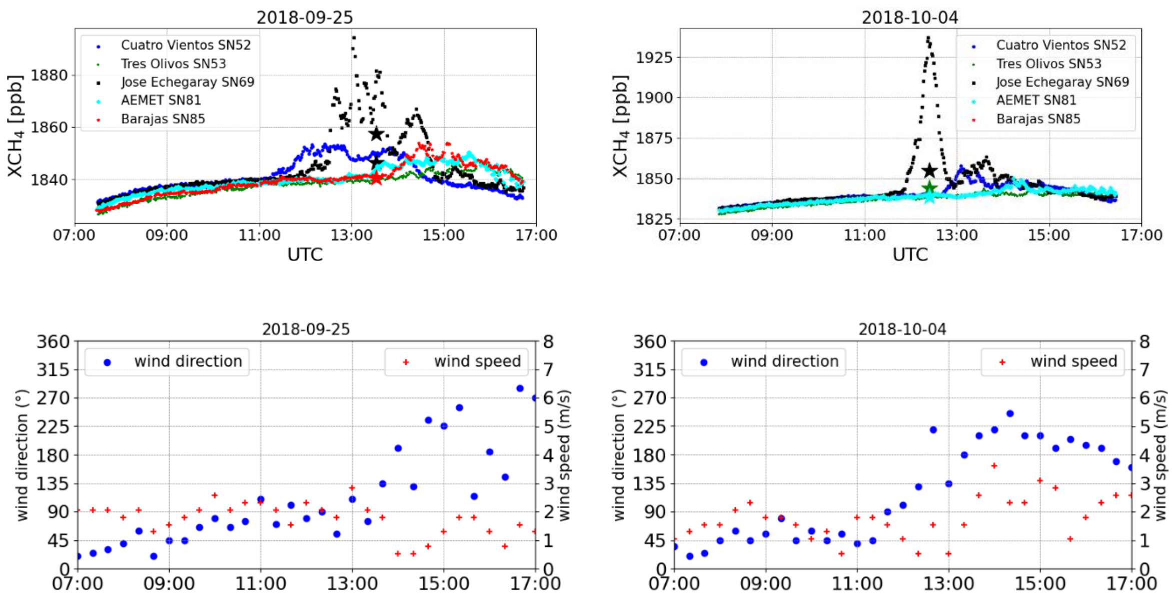

Figure 4: Time series of COCCON measurements at five stations on two days in 2018. Star symbols represent the averaged TROPOMI observations within a radius of 5 km around each station. Lower panels show the wind direction and wind speed measured at the Cuatro Vientos Airport.

TROPOMI detected 10 ppb higher XCH_4 at Jose Echegaray station than at Barajas station on September 25, 2018. However, COCCON observed a much higher amount of XCH_4 (53 ppb) at Jose Echegaray station than at Barajas station (and other stations) at around 13:00 UTC. The delayed enhancements at AEMet and Barajas stations at the downwind direction are found after the wind direction changed from north more towards south direction. Another obvious enhancement of XCH_4 is observed at Jose Echegaray station by the COCCON SN69 instrument at around 12:30 on October 4, 2018, with about 97 ppb higher XCH_4 than COCCON measurements at the other four stations. However, TROPOMI only measured about 13 ppb higher XCH_4 at Jose Echegaray station compared to the TROPOMI measurements at the other stations. These considerable enhancements at Jose Echegaray station observed by the COCCON instrument are likely due to the local source (the nearby Valdemingómez waste plant). The plume is in close vicinity to the source narrower than the pixel scale of the satellite, and therefore is only detected as an attenuated signal by TROPOMI. The full width at the half maximum (FWHM) of the enhancement peak on October 4, 2018 roughly covers a temporal window ~~time period~~ of 30min, with a corresponding wind direction change of 22.5°

(~0.4 rad) and an averaged wind speed of 1.0 m s^{-1}. The distance between the COCCON SN69 to the Valdemingómez waste plant is about 4500 m. The 97 ppb enhancement measured by COCCON SN69 instrument yields an estimated emission strength of 3.7×10^{25} molec s^{-1}.

According to the Spanish Register of Emissions and Pollutant Sources (PRTR, http://www.en.prtr-es.es/, last access: 20 February, 2021), more than 95% of total CH_4 emissions are from three waste treatment and disposal plants in the Madrid region (locations showed in Figure 1). The annual CH_4 emission rates from the PRTR for each plant are listed in Table 2. The total emission strength for each plant is about 2.5×10^{25} molec s^{-1}. This value only considers the "cells" in production, i.e. those where the waste is not yet covered with soil. The emissions from sealed cells are not included in the total emissions, but they still emit CH_4 for ~~during some~~ years after sealing. So, the estimated emission rates from the inventories are expected to underestimate the true emissions, which fits reasonably with the estimated emission rate derived from COCCON measurements. The COCCON instruments show a very good ability to detect the source. Based on this evidence we investigate the potential of the TROPOMI and IASI CH_4 products for detecting CH_4 sources in the following.

Table 2: CH_4 emission rates in three waste treatment and disposal plants in Madrid from PRTR.

Waste treatment and disposal plants	Valdemingómez (molec s^{-1})	Pinto (molec s^{-1})	Alcalá (molec s^{-1})	Total (molec s^{-1})
2017	7.4×10^{24}	1.2×10^{25}	2.1×10^{24}	2.2×10^{25}
2018	7.4×10^{24}	1.3×10^{25}	2.1×10^{24}	2.2×10^{25}
2019	9.8×10^{24}	1.4×10^{25}	9.4×10^{23}	2.5×10^{25}

3.2 Predominant wind

To better represent~~ing~~ the whole area of Madrid, the hourly ERA5 model wind at a height of 10 m around Madrid is used. ERA5 is the fifth generation climate reanalysis produced by the European Centre for Medium-range Weather Forecasts (ECMWF) (Copernicus Climate Change Service, 2017). The TROPOMI overpasses over Madrid cover the time range from 12:00 UTC – 14:30 UTC (IASI overpasses are typically from 09:30 UTC – 10:30 UTC), but the dispersion of emitted CH_4 is influenced by the ground conditions (e.g. wind speed and wind direction) over a wider time range (Delkash et al., 2016; Rachor et al., 2013). Therefore, the wind information between daytime (08:00 UTC – 18:00 UTC) is chosen to define the predominant wind direction for each day. Figure 5 presents the wind roses for daytime between 10 November 2017 and 10 October 2020 (the first and last day with valid TROPOMI data). The dominating wind direction was southwesterly. To the northwest of Madrid are the Guadarrama mountains located and the Jarama and Manzanares river basins, which influence the air flow. Therefore, we use a wider wind range for the specific wind area in this study to cover the dominant wind directions, i.e. SW for the range of 135° – 315° and NE for the remaining direction. If a wind direction dominates 60% of records for one day, i.e., if the wind direction belongs to one specific area more than 60% of the daytime (08:00 UTC – 19:00 UTC), then this predominant wind direction is selected for that day. The SW and NE wind fields are used for constructing wind-assigned anomalies in this study and we will demonstrate this construction by using TROPOMI nitrogen dioxide (NO_2) data in the next section. Table 3 summaries the number of days and wind speed for each specific wind area. The wind direction during the TROPOMI overpasses was 61.8% in SW wind field and 28.4% in NE wind field and their averaged wind speed is similar.

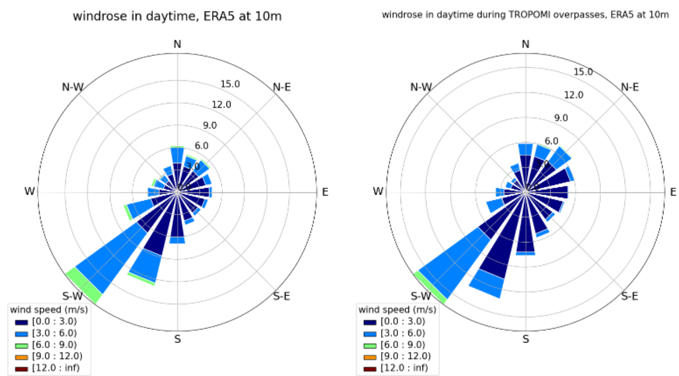

Figure 5: Wind roses for daytime (08:00 UTC – 19:00 UTC) from 10 November 2017 to 10 October 2020 for the ERA5 model wind. The left panel covers all days and the right panel covers the days with TROPOMI overpasses.

Table 3: Number of days and the averaged ERA5 wind speed (± standard deviation) per specific wind area in daytime (08:00 UTC – 18:00 UTC) from 10 November 2017 to 10 October 2020. Columns 2 and 3 are for all days, and columns 4 and 5 are for days with TROPOMI overpass.

			TROPOMI overpass	
Wind direction range	**Number of days in total (%)**	**Averaged wind speed ± standard deviation (m s^{-1})**	**Number of days in total (%)**	**Averaged wind speed ± standard deviation (m s^{-1})**
NE / >315° or <135°	30.4	2.6 ± 1.5	28.4	2.3 ± 1.2
SW / 135° – 315°	68.4	2.8 ± 1.7	61.8	2.3 ± 1.4

3.3 Demonstration of the wind-assigned anomaly method

When fossil fuels are burned, nitrogen monoxide (NO) is formed and emitted into the atmosphere. NO reacts with O_2 to form NO_2 and with ozone (O_3) to produce O_2 and NO_2. NO_2 is an extremely reactive gas with a short lifetime of a couple of hours and has lower background levels than CH_4 (Kenagy et al, 2018; Shah et al., 2020). It is measured by TROPOMI with excellent quality. Therefore, it is a suitable proxy for demonstrating the method developed for the wind-assigned anomaly.

TROPOMI offers simultaneous observations of NO_2 columns. The recommended quality filter value for the analysis of TROPOMI NO_2 columns is qa>0.75 (http://www.tropomi.eu/sites/default/files/files/publicSentinel-5P-Level-2-Product-User-Manual-Nitrogen-Dioxide.pdf). Based on the predominant wind direction in Madrid (see section 3.2), the averaged wind-assigned anomalies are defined here as the difference of the mean TROPOMI NO_2 column under the wind direction from NE and the mean TROPOMI NO_2 column under the predominant wind direction of SW in Madrid.

Figure 6 (a) illustrates the wind-assigned anomalies of TROPOMI NO_2 (ΔNO_2) on a 0.1° × 0.135° latitude/longitude grid during 2018 – 2019. Pronounced fusiform-shaped plumes are observed along NE – SW wind direction as expected. Figure 6 (b) shows the wind-assigned anomalies derived from the simple model introduced in Sect. 2.3, using Madrid city center as the point source with an assumed emission rate (ε) of 5.0×10^{24} molec s^{-1} and using ERA5 10 m wind data. The similar symmetrical positive and negative plumes to those in Figure 6 (a) imply that our method of wind-assigned anomaly is working as anticipated, and that the ERA5 10 m data are indeed representative for the area and that the implementation of the satellite data analysis is correct. Figure 6 (c) shows the strong correlation between the wind-assigned anomalies derived from the TROPOMI measurements and the simple plume model ($\varepsilon = 5.0\times10^{24}$ molec s^{-1}). Using the fitting method as described in Sect. B.2, we estimate an emission rate of 3.5×10^{24} molec s^{-1} ± 3.9×10^{22} molec s^{-1}. Here the uncertainty is due to the noise of the observations and is calculated according to Eq. 21 (Appendix B). This estimated source strength is weaker than the strength obtained by Beirle et al. (2011), where the reported NO_x emission is around 150 mol s^{-1} in Madrid, corresponding to a NO_2 emission of 6.8 $\times10^{25}$ molec s^{-1}. It is because our model does not consider the decay of NO_2, which results in a lower emission rate.

The result of this test using NO_2 also allows the used angular spread parameter in the plume model to be adjusted (see Section 2.3 and Eq. 3). As it can be seen from Figure A- 1, assuming an angular spread of 60° reasonably reproduces the shape of the plume.

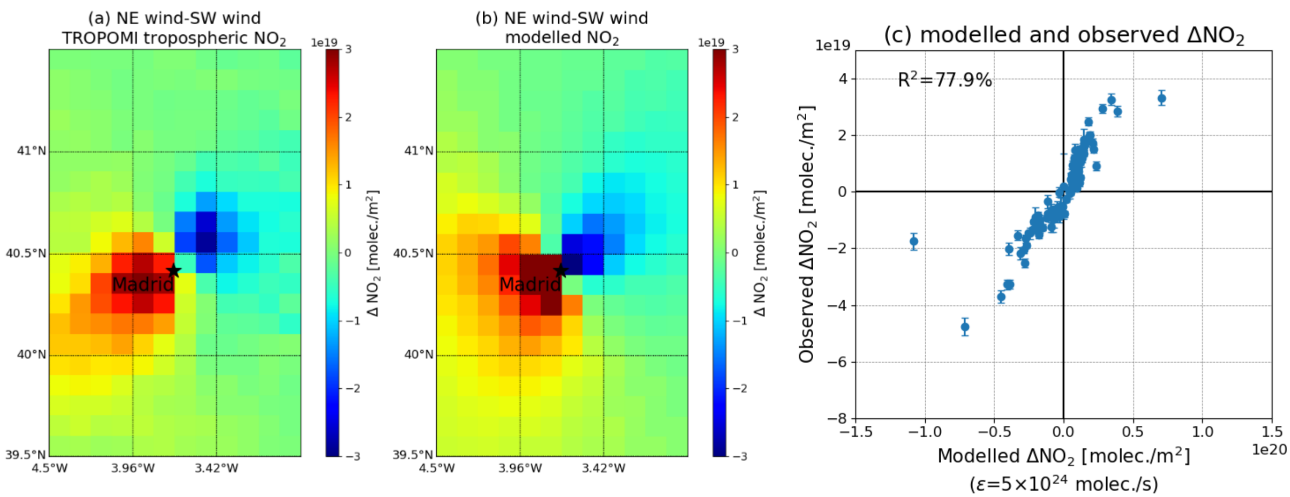

Figure 6: Wind-assigned anomalies derived from (a) TROPOMI tropospheric NO_2 column, (b) our simple plume model (ε= 5×10^{24} molec s^{-1}) over Madrid in NE - SW direction on a 0.1° × 0.135° latitude/longitude grid during 2018 – 2020, and (c) shows the correlation plot between observed ΔNO_2 and modelled ΔNO_2 (ε=5×10^{24} molec s^{-1}) during 2018-2019.

3.4 XCH_4 and $TXCH_4$ anomaly

CH_4 has a relatively longer lifetime ~~than~~ as compared to NO_2 and its background in the atmosphere is high. An increasing trend with obvious seasonality and strong day-to-day signals for XCH_4 is seen in Figure 7 (upper panels). Therefore, these background signals need to be removed before simulating the wind-assigned anomalies (see Sect. B.1). After removing the background, the anomalies (raw data - background) represent more or less the emission from local area (Figure 7 lower panels).

Figure 8 illustrates the anomalies of XCH_4, $TXCH_4$ and $UTSXCH_4$ for all measurement days, days with predominating SW wind field and days with predominating NE wind field. The distributions over the whole area for XCH_4 and $TXCH_4$ are similar and no obvious enhancement is observed in $UTSXCH_4$, as expected, since CH_4 abundances dominate in the troposphere. The areas where the three waste plants are located show obvious high anomalies in the figures (Figure 8 a and d) when the data are averaged over all days for all wind directions, and in downwind direction (Figure 8 b, c, e and f), demonstrating that our method of removing the background works well and the satellite products can detect the local pollution sources after removing the background. Enhanced plumes of XCH_4 and $TXCH_4$ are better visible on the downwind side of SW than on the downwind side of NE wind field. This is because SW is the most dominant wind direction and the SW plume signal is based on a higher number of data and thus less noise.

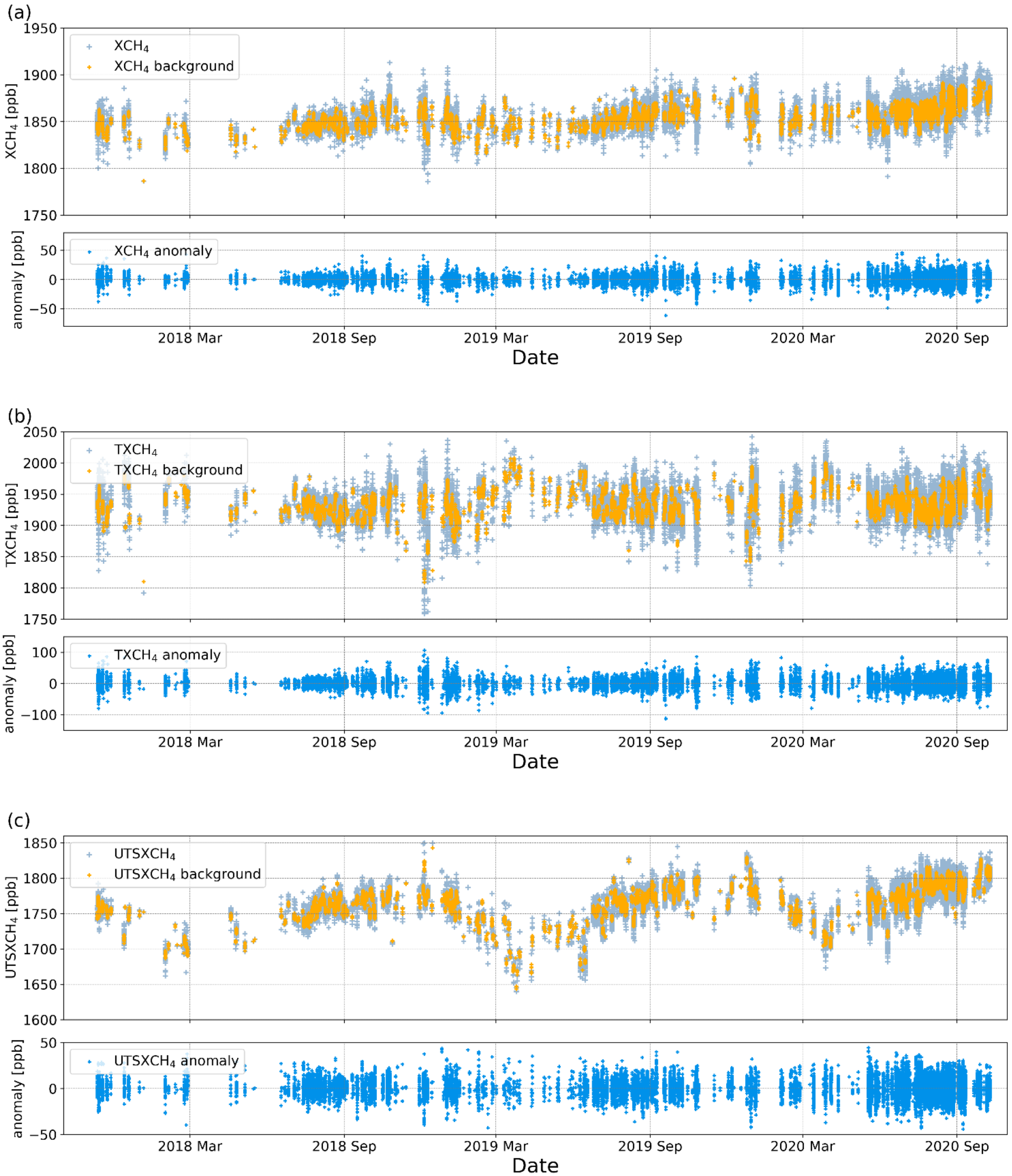

Figure 7: Time series of (a) XCH_4, (b) $TXCH_4$ and (c) UTS XCH_4, showing raw data and background in each upper panel and anomalies in each corresponding lower panel.

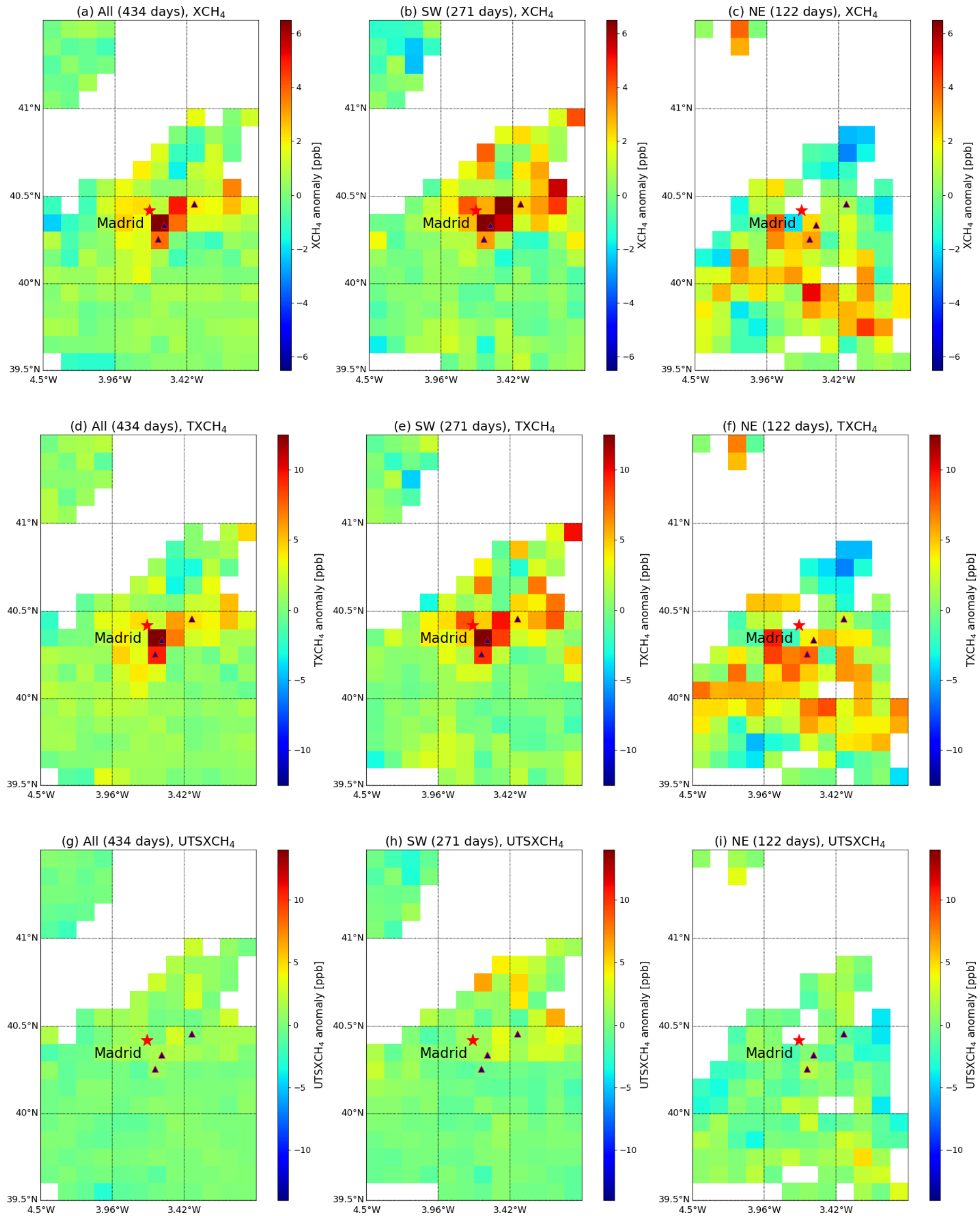

Figure 8: (a-c) XCH$_4$, (d-f) TXCH$_4$ and (g-i) UTSXCH$_4$ anomalies averaged for all days, days with SW wind and NE wind directions. The triangle symbols represent the location of waste plants.

3.5 Estimation of CH_4 emission strengths from satellite data sets

The wind-assigned anomalies derived from XCH_4 anomalies and $TXCH_4$ anomalies on a 0.1° × 0.135° latitude/longitude grid are presented in Figure 9. The XCH_4 and $TXCH_4$ wind-assigned anomalies show similar bipolar plumes but are more disturbed compared to those derived from NO_2. This is because the CH_4 signal is weak compared to the background concentration, so the noise level of the measurement and the imperfect elimination of the background are significant disturbing factors.

Based on the knowledge of the locations of the three waste plants, we choose their locations as point sources to model the enhanced XCH_4 according to the wind information. The initial emission strength is 1×10^{26} molec s^{-1} in total and the emission rate at each point source is repartitioned among these three sites according to Table 2. The modelled and observed wind-assigned anomalies show a reasonable linear correlation (coefficient of determination R^2 of about 49% and 44% for XCH_4 and $TXCH_4$, respectively) with observed ΔXCH_4. Based on Eq. 18 (Appendix B), we obtained an estimated emission rate of $7.4\times10^{25} \pm 6.4\times10^{24}$ molec s^{-1} for XCH_4 and $7.1\times10^{25} \pm 1.0\times10^{25}$ molec s^{-1} for $TXCH_4$. The uncertainty values given here are the square root sum of the uncertainty due to the background signal and the data noise, which are calculated according to Eq. 20 and 21. Figure 9 (g), (h) and (i) show the wind-assigned anomalies for $UTSXCH_4$. For the modelled $UTSXCH_4$ anomalies we assume here the CH_4 enhancement to occur at altitudes between 7 and 20 km a.s.l. As expected, the fit of these model data to the observed $UTSXCH_4$ data yields emission rates ~~of~~ close to zero ($1.4\times10^{25} \pm 7.2\times10^{24}$ molec s^{-1}), revealing that there is no significant plume signal above 7 km a.s.l. The fact that for $TXCH_4$ we obtain practically the same emission rates as for XCH_4 and that in the $UTSXCH_4$ data we see almost no plume nicely proves the quality of our careful background treatment method and the low level of cross-sensitivity between the $TXCH_4$ and $UTSXCH_4$ data products. The applied background treatment allows detecting the surface-near emission signal consistently in the total column XCH_4 data and in the tropospheric $TXCH_4$ data.

Figure 10~~Figure 10~~ illustrates the estimated emission strengths for the different products. The emission strengths derived from the satellites are higher than the ones derived from COCCON measurements, as TROPOMI covers a larger area while COCCON measurements are only sensitive to local sources from the nearby waste plant. The PRTR inventory document gives lower values than our results. This is probably because it only lists the active landfill cells and does not include the closed ones in Madrid, which probably still emit for many years (Sánchez et al., 2019).

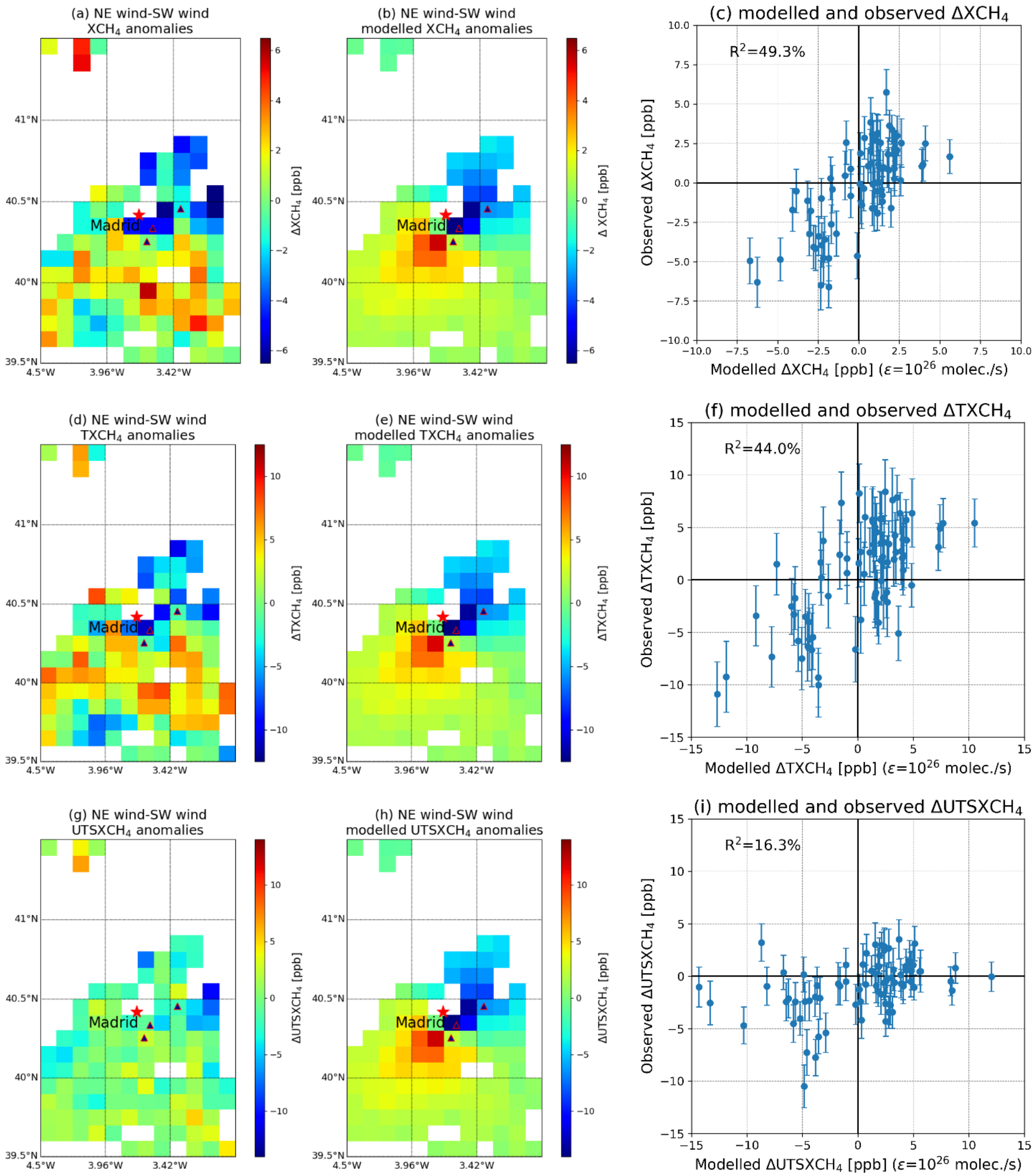

Figure 9: Wind-assigned XCH_4 plume derived from (a) TROPOMI XCH_4 anomalies, (d) synergetic $TXCH_4$ anomalies and (g) $UTSXCH_4$ anomalies and their corresponding modeled plume (b, e, h) over Madrid in NE – SW direction on a 0.1° × 0.135° latitude/longitude grid. The correlation plots between observed ΔXCH_4 and modelled ΔXCH_4 ($\varepsilon=1\times10^{26}$ molec s^{-1}) for different products (c, f, i). Here we use the three waste plants as the point sources (blue triangle with red edge color). The initial emission rate in the plume model is 1×10^{26} molec s^{-1}. This value is proportionally distributed into three point sources based on the a priori knowledge of emission rate in each waste plant. For the modelled $UTSXCH_4$ anomalies we assume the CH_4 enhancements to occur at altitudes between 7 and 20 km a.s.l.

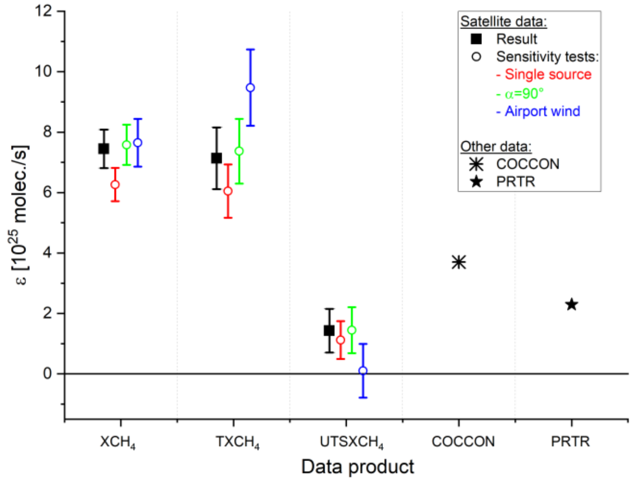

Figure 10: Emission strengths for the different products and for the sensitivity tests. Also included are the COCCON observations which characterize the Valdemingómez waste plant contribution and the total of all three sources according to the PRTR inventory.

3.6 Sensitivity study for emission strength estimates

The point sources and their proportion in the total emission rate in this study are based on the a priori knowledge of three different waste plant locations. If we use a single source located at the Pinto waste disposal site only, it yields an emission rate of 6.3×10^{25} molec s^{-1}, ~15% lower than that of the three-point sources for CH_4 and 6.0×10^{25} molec s^{-1} (-15%) for tropospheric CH_4 (see Figure 10~~Figure 10~~). The opening angle (α) is experimentally selected based on the comparison between the TROPOMI measured and modelled NO_2 plume, which results in some uncertainties as well. Using 90° instead of 60° for α in the plume model results in an emission strength of 7.6×10^{25} molec s^{-1} (+3% change) for CH_4 and of 7.4×10^{25} molec s^{-1} (+4% change) for tropospheric CH_4.

The surface wind can be influenced by the topography and the actual transport pathway from emission source to the measurement station is difficult to know (Chen et al., 2016; Babenhauserheide et al., 2020). To study the wind sensitivity, the hourly wind information measured at the Cuatro Vientos Airport at 10m height is used instead of the ERA5 10 m wind. There are other in situ measurements available but not used here, as the AEMet Headquarter station is affected by nearby buildings and the Barajas Airport station is very close to a river (Jarama) that determines a specific wind pattern. The wind measured at the Cuatro Vientos Airport is quite different compared to the ERA5 wind, as in situ measured NE wind becomes dominant as well and the wind speed in SW wind field increases by ~50% compared to that of ERA5 wind (Figure A- 3, Figure A- 4 and Table A- 1). Using the wind measured at the Cuatro Vientos Airport results in an emission rate of 7.7×10^{25} molec s^{-1} (+4%) for CH_4 and 9.5×10^{25} molec s^{-1} (+34%) for tropospheric CH_4.

In summary, the uncertainties derived from the source location, opening angle or wind cannot be ignored, but nevertheless the emission rates estimated from the space-borne observations are clearly larger than the values reported in Table 2 and are larger than the ones estimated from the COCCON SN69 observations in October 2018.

4 Conclusions

The present study analyzes TROPOMI XCH_4 and IASI CH_4 retrievals over an area around Madrid for more than 400 days within a rectangle of 39.5°N – 41.5°N and 4.5°W – 3.0°W (125 km × 220 km) from 10 November 2017 until 10 October 2020. During this time period, a two-week field campaign was conducted in September 2018 in Madrid, in which five ground-based COCCON instruments were used to measure XCH_4 at different locations around the city center.

First, TROPOMI XCH_4 is compared with co-located COCCON data from the field campaign, showing a generally good agreement, even though the radius of the collection circle for the satellite measurements was as small as 5 km. However, there are six days when obvious enhancements due to local sources were observed by COCCON around noon at the most southeast station (Jose Echegaray), which were underestimated by TROPOMI. The ground-based COCCON observations indicate a local source strength of 3.7×10^{25} molec s^{-1} from observations at Jose Echegaray station on October 4, 2018, which is reasonable compared to the emissions assumed for nearby waste plants. The waste plant locations are later used as the point sources to model the emission strength for CH_4.

According to the ERA5 model wind at 10 m height, SW (135° – 315°) winds (NE covering the remaining wind field) are dominant in the Madrid city center in the time range from November 2017 to October 2020. Based on this wind information, the wind-assigned anomalies are defined as the difference of satellite data between the conditions of NE wind field and SW wind field. We use the simultaneously measured tropospheric NO_2 column amounts from TROPOMI as a proxy to evaluate the wind-assigned anomaly approach due to its short lifetime, and clear plume shape, by using ERA5 model wind. Pronounced and bipolar NO_2 plumes are observed along the NE – SW wind direction and a tropospheric NO_2 emission strength of 3.5×10^{24} $\pm$ 3.9×10^{22} molec s^{-1} is estimated. This implies that our method of wind-assigned anomaly is working reliably, and that the ERA5 wind data used are indeed representative ~~for~~ of the area and the implementation of the satellite data analysis is correct.

CH_4 ~~has a long lifetime~~ is a long-lived gas and so there are strong CH_4 background signals in the atmosphere. Therefore, the background values need to be removed and the anomalies have to be determined before calculating emission strengths. In this study, the removed background values include linear increase, seasonal cycle, daily variability and horizontal variability. The areas where the three waste plants are located show obvious high anomalies, demonstrating that satellite measurements can detect the local sources after removing the background. Enhanced plumes are more pronounced in the downwind side of SW, whereas the observed downwind plume signal for NE wind is noisier, partly due to the lower number of NE wind situations.

The wind-assigned TROPOMI XCH_4 anomalies show a less clear bipolar plume than NO_2. This is because CH_4 has a long lifetime and its high background is difficult to be totally removed. Based on the wind-assigned anomalies, the emission strength estimated from the TROPOMI XCH_4 data is 7.4×10^{25} $\pm$ 6.4×10^{24} molec s^{-1}. In addition, this method is applied to the tropospheric partial column-averaged (ground – 7 km a.s.l.) dry-air molar fractions of methane ($TXCH_4$, obtained by combing TROPOMI and IASI products) yielding an emission strength of 7.1×10^{25} $\pm$ 1.0×10^{25} molec s^{-1}. We show that in the upper troposphere/stratosphere there is no significant plume signal (1.4×10^{25} $\pm$ 7.2×10^{24} molec s^{-1}). The estimation of very similar emission rates from XCH_4 and $TXCH_4$ together with the estimated negligible emission rates when using data representing the upper troposphere/stratosphere proves the robustness of our method. The emission rates derived from satellites (XCH_4 and $TXCH_4$) are higher than that derived from COCCON observations, as satellites cover larger areas with other CH_4 sources and COCCON likely measures local sources.

The surface wind is easily influenced by the topography, which introduces uncertainties in the estimated emission strengths. Using in situ measured wind at the Cuatro Vientos Airport instead of ERA5 model wind results in an estimated emission rate of 7.7×10^{25} molec s^{-1} (+4%) for CH_4 and 9.5×10^{25} molec s^{-1} (+34%) for tropospheric CH_4. Uncertainties can as well be caused by the choice of the opening angle in the plume model. The estimated emission rates with α=90° are 7.6×10^{25} molec s^{-1} (+3%) for CH_4 and of 7.4×10^{25} molec s^{-1} (+4%) for tropospheric CH_4. When using a single source located in the Madrid city center, the emission strengths are 6.3×10^{25} molec s^{-1} (-15%) for CH_4 and 6.0×10^{25} molec s^{-1} (-15%) for tropospheric CH_4.

In summary, in this study for the first time TROPOMI observations are used together with IASI observations and the ground-based COCCON observations to investigate CH_4 emissions from landfills in an important metropolitan area like Madrid. The COCCON instruments show a promising potential for satellite validation and an excellent ability for observation of local sources. The data presented here shows that TROPOMI is able to detect the tropospheric NO_2 and XCH_4 anomalies over metropolitan areas with support from meteorological wind analysis data. ~~As outlook, this~~This methodology could also be applied to other source regions, space-based sensors and sources of CO_2.

Data availability. The data are accessible by contacting the corresponding author (qiansi.tu@kit.edu). The SRON S5P-RemoTeC scientific TROPOMI CH4 dataset from this study is available for download at https://doi.org/10.5281/zenodo.4447228 (Lorente et al., 2021, last access: 06 May 2021). The TROPOMI data set is publicly available from https://scihub.copernicus.eu/ (last access: 06 May 2021; ESA, 2020). The access and use of any Copernicus Sentinel data available through the Copernicus Open Access Hub are governed by the legal notice on the use of Copernicus Sentinel Data and Service Information, which is given here: https://sentinels.copernicus.eu/documents/247904/690755/Sentinel_Data_Legal_Notice (last access: 06 May 2021; European Commission, 2020). The MUSICA IASI data set is available for download via https://doi.org/10.35097/408 (Schneider et al. 2021c).

Author contributions. Qiansi Tu, Frank Hase and Omaira García developed the research question. Qiansi Tu wrote the manuscript and performed the data analysis with input from Frank Hase, Omaira García, Matthias Schneider and Farahnaz Khosrawi. Frank Hase suggested the method of constructing wind-assigned anomalies for source quantification. Matthias Schneider suggested the method for calculating the anomalies, for fitting the emission rates and estimating the uncertainty. Omaira García provided the COCCON and meteorological data and helped to interpret it. Tobias Borsdorff and Alba Lorente supported technically for the TROPOMI data analysis. Matthias Schneider, Benjamin Ertl and Christopher J. Diekmann provided the combined (MUSICA IASI + TROPOMI) data and supported technically for the analysis of these data. All other coauthors participated in the field campaign and provided the data. All authors discussed the results and contributed to the final manuscript.

Competing interests. The authors declare that they have no conflict of interest.

Acknowledgements. We acknowledge ESA support through the COCCON-PROCEEDS and COCCON-PROCEEDS II projects. In addition, this research was funded by the Ministerio de Economía y Competitividad from Spain through the INMENSE project (CGL2016-80688-P). This research has largely benefit from funds of the Deutsche Forschungsgemeinschaft (provided for the two projects MOTIV and TEDDY with IDs/290612604 and 416767181, respectively). Important part of this work was performed on the supercomputer ForHLR funded by the Ministry of Science, Research and the Arts Baden-Württemberg and by the German Federal Ministry of Education and Research.

We acknowledge the support by the Deutsche Forschungsgemeinschaft and the Open Access Publishing Fund of the Karlsruhe Institute of Technology.

Appendix A

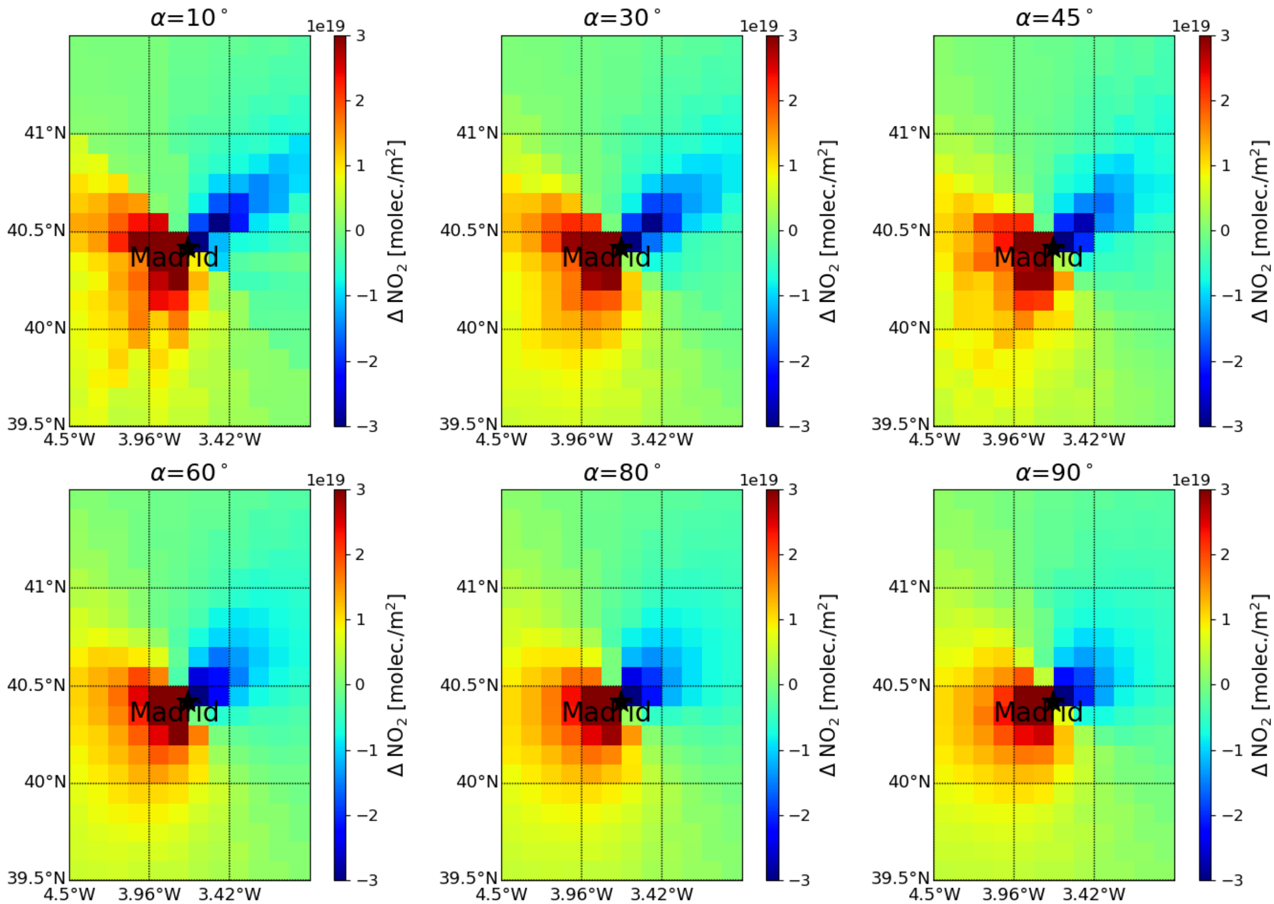

Figure A- 1: Examples of wind-assigned NO_2 plume based on the simple plume model (ε = 5.0×10^{24} molec s^{-1}) using Madrid as the point source in NE – SW direction on a 0.1° × 0.135° latitude/longitude grid with different opening angle (α) from 10° to 90°.

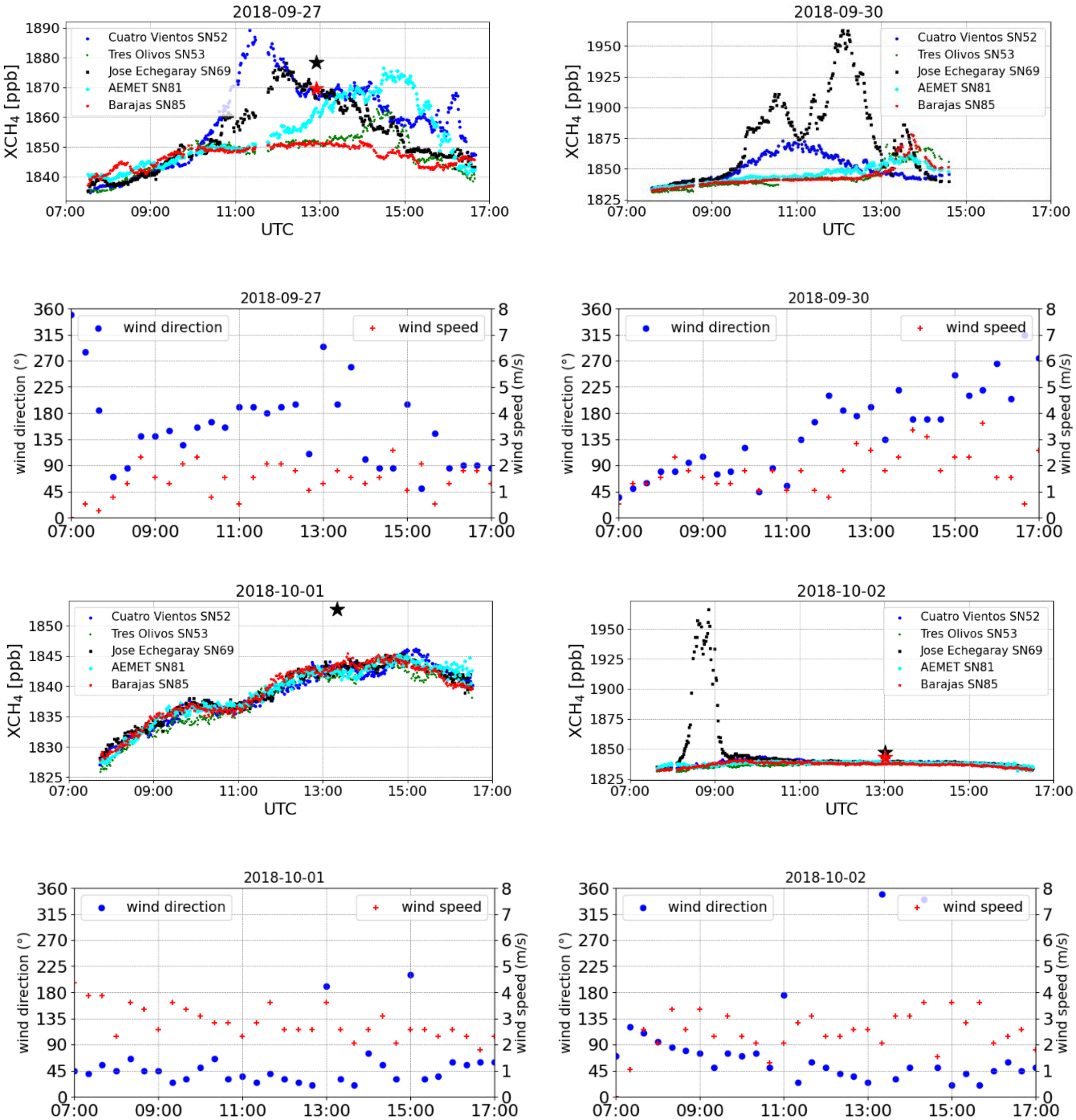
2018-09-27
2018-09-30
2018-10-01
2018-10-02
Cuatro Vientos SN52
Tres Olivos SN53
Jose Echegaray SN69
AEMET SN81
Barajas SN85
XCH4 [ppb]
UTC
wind direction
wind speed
wind direction (°)
wind speed (m/s)

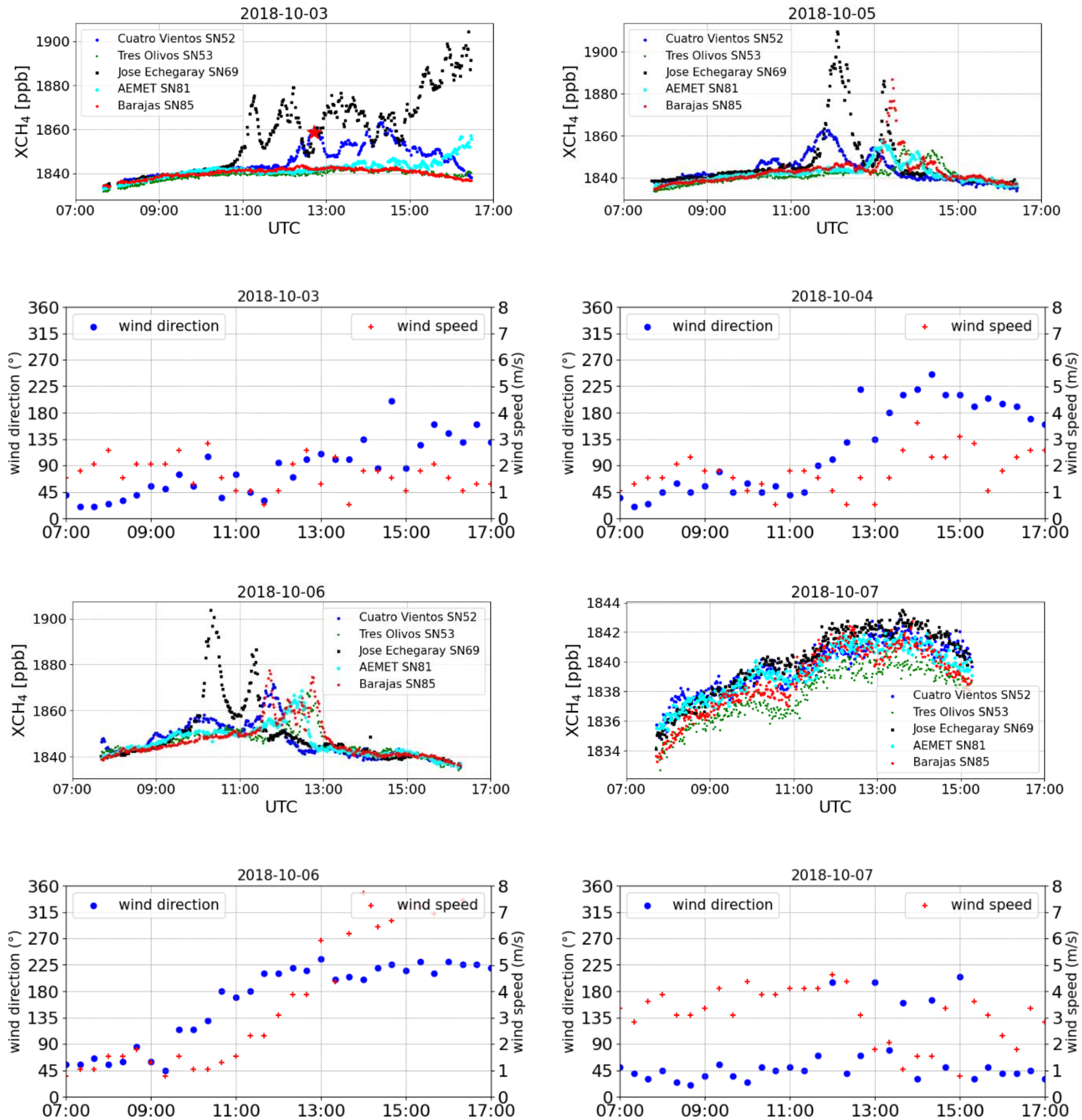

Figure A- 2: Time series of COCCON measurements at five stations and corresponding time series of wind fields (direction and speed) measured at the Cuatro Vientos Airport on eight days during MEGEI-MAD campaign in 2018. Star symbols represent the TROPOMI observations within a radius of 5 km around each station.

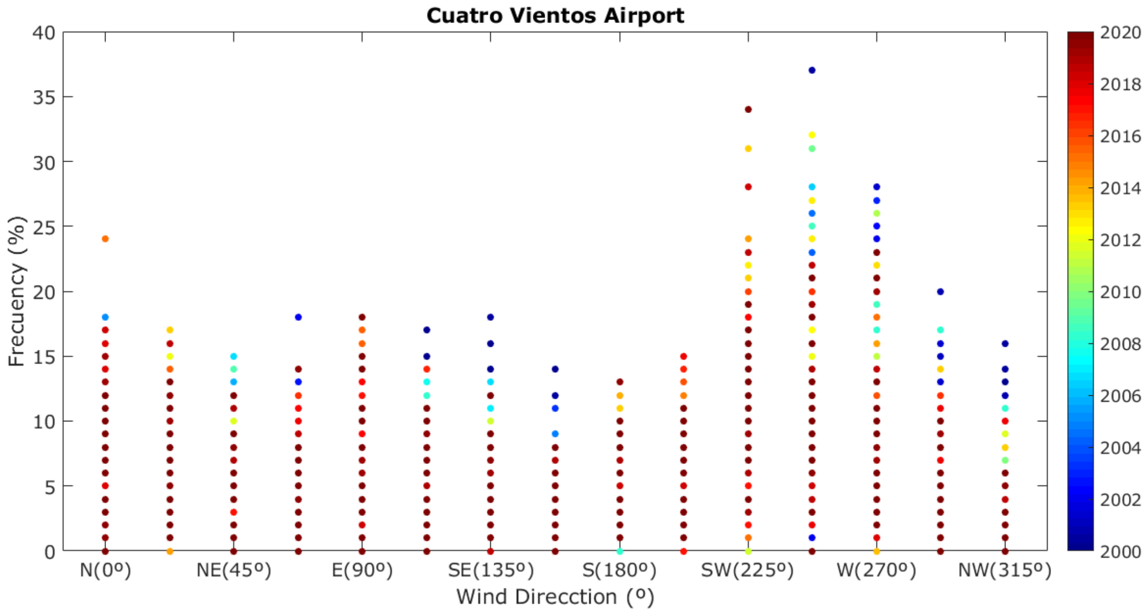

Figure A- 3: Percentage of occurrence for wind direction measured at the Cuatro Vientos Airport between 2000 and 2020. The predominant wind direction is southwest and up to 35% of time ~~(personal communication of Omaira García)~~.

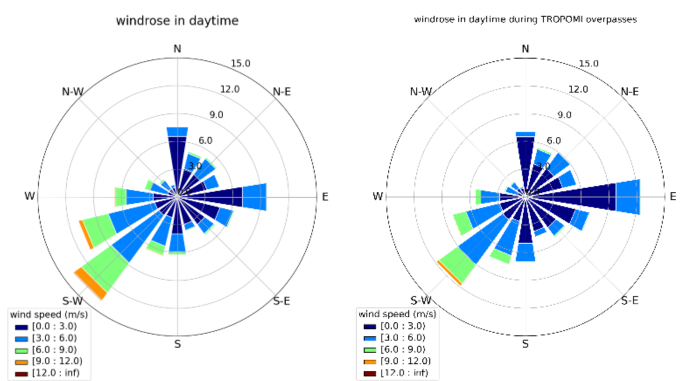

Figure A- 4: Wind roses for daytime (08:00 UTC – 19:00 UTC) from 10 November 2017 to 11 September 2020 from the wind measurements at the Cuatro Vientos Airport. The left panel covers all days and the right panel covers the days with TROPOMI overpasses.

Table A- 1: Number of days and the averaged wind speed (± standard deviation) per specific wind area in daytime (08:00 UTC – 18:00 UTC) from 10 November 2017 to 11 September 2020 measured at the Cuatro Vientos Airport. Columns 2 and 3 are for all days, and columns 4 and 5 are for days with TROPOMI overpass.

Wind direction range	Number of days in total (%)	Averaged wind speed ± standard deviation (m s^{-1})	TROPOMI overpass Number of days in total (%)	TROPOMI overpass Averaged wind speed ± standard deviation (m s^{-1})
NE / >315° or <135°	35.4	2.4 ± 1.5	36.0	2.2 ± 1.3
SW / 135° – 315°	49.3	4.2 ± 2.5	44.4	3.4 ± 2.1

Appendix B

B.1 CH_4 background signal

The satellite data can be written as a vector **y**, where each element corresponds to an individual satellite data point. This signal is caused by a CH_4 background signal and the CH_4 plume due to the emissions from the waste disposal sites near Madrid:

$$\boldsymbol{y} = \boldsymbol{y_{BG}} + \boldsymbol{y_{plume}} \quad \textbf{Eq. 7}$$

It is of great importance to adequately separate both components for estimating the emission strength from the satellite data.

For determining the background signal ($\boldsymbol{y_{BG}}$), we setup a background model:

$$\boldsymbol{M_{BG}} = \boldsymbol{y_{BG}} = \mathbf{K_{BG}}\boldsymbol{x_{BG}} \quad \textbf{Eq. 8}$$

The matrix $\mathbf{K_{BG}}$ is a Jacobian matrix that allows to reconstruct the background according to a few background model coefficients (the elements of the vector $\boldsymbol{x_{BG}}$). We also create a Jacobian $\mathbf{K^*_{BG}}$, which is the same as $\mathbf{K_{BG}}$ but set to zero for observations where the wind data suggest a significant impact of the CH_4 plume on the satellite data. The calculations of the plume CH_4 signals are made according to Sect. 2.3. With the use of $\mathbf{K^*_{BG}}$ we make sure that the estimated background signal is not affected by the CH_4 plume.

The ~~Jacobian matrix~~ $\mathbf{K_{BG}}$ is a Jacobian matrix where each row represents an individual satellite observation and each column a component of the background model. The background model considers a smooth background, which is a constant CH_4 value, a linear increase with time and a seasonal cycle described by the amplitude and phase of the three frequencies 1/year, 2/year, and 3/year. Furthermore, we fit a daily anomaly, which is the same for all data measured during a single day and a horizontal anomaly, which is the same for any time but dependent on the horizontal location. For the latter we use a 0.1° × 0.135° (latitude × longitude) grid.

We invert the problem in order to estimate the background model coefficients (elements of the vector $\boldsymbol{x_{BG}}$):

$$\boldsymbol{\hat{x}_{BG}} = \mathbf{G_{BG}}\boldsymbol{y} \quad \textbf{Eq. 9}$$

With $\mathbf{G_{BG}}$ being the so-called gain matrix

$$\mathbf{G_{BG}} = (\mathbf{K^*_{BG}}^{\boldsymbol{T}}\boldsymbol{S_{y,n}}^{-1}\mathbf{K^*_{BG}} + \boldsymbol{S_a}^{-1})^{-1}\mathbf{K^*_{BG}}^{\boldsymbol{T}}\boldsymbol{S_{y,n}}^{-1} \quad \textbf{Eq. 10}$$

Because $\mathbf{K^*_{BG}}$ **(and thus $\mathbf{G_{BG}}$) is set to zero whenever $\boldsymbol{y_{plume}} = 0$**, we can use in Eq. 9 $\boldsymbol{y}$ instead of $\boldsymbol{y_{BG}}$. The matrix $\boldsymbol{S_{y,n}}$ stands for the noise covariance of the satellite data. For constraining the problem, we use a diagonal $\boldsymbol{S_a}^{-1}$ (no constraint between different coefficients) with a very low constraint value for the coefficient determining the constant and higher constraint values for the other coefficients. For calculating the uncertainty of the background signal, we calculate the vector $\boldsymbol{y} - \mathbf{K^*_{BG}}\boldsymbol{\hat{x}_{BG}}$ and then the mean square value from its elements that represent observations not affected by the plume. This mean square value is then used as the diagonal entries of the diagonal matrix $\boldsymbol{S_{y,BG}}$. ~~Here we use $\boldsymbol{S_{y,BG}}$ as the diagonal matrix with the mean square value of the difference $\boldsymbol{y_{BG}} - \mathbf{K^*_{BG}}\boldsymbol{\hat{x}_{BG}}$ being the diagonal elements.~~ In this context, $\boldsymbol{S_{y,BG}}$ considers the deficits of the background model and the uncertainty in the background if determined from data with a certain noise level. As an alternative, we could use modeled high resolution XCH_4 fields (e.g. from CAMS high resolution greenhouse gas forecast

(Barré et al., 2021)) for these calculations. We can assume that the model data has no noise and perform an exclusive estimation of the deficits of the background model calculation in form of a full $S_{y,BG}$ covariance matrix. This more sophisticated uncertainty estimation can be a task for future work.

The uncertainty of the background model coefficients can be calculated as:

$$\mathbf{S}_{\hat{x}_{BG}} = \mathbf{G}_{\mathbf{BG}} \boldsymbol{S}_{y,BG} \mathbf{G}_{\mathbf{BG}}{}^{T} \qquad \textbf{Eq. 11}$$

For each day there is an uncertainty in the background coefficients and the uncertainty is correlated with the uncertainty at other days. All this information is provided in the uncertainty covariance $\mathbf{S}_{\hat{x}_{BG}}$.

With the full Jacobian $\mathbf{K}_{\mathbf{BG}}$ we can now model the background for the measurement state (also for the measurements that are assumed to be affected by the CH_4 waste disposal plume):

$$\boldsymbol{y}_{BG} = \mathbf{K}_{\mathbf{BG}} \cancel{\mathbf{K}} \hat{\boldsymbol{x}}_{BG} \qquad \textbf{Eq. 12}$$

and calculate the plume signal according to Eq. 7 as:

$$\boldsymbol{y}_{plume} = \boldsymbol{y} - \mathbf{K}_{\mathbf{BG}} \cancel{\mathbf{K}} \hat{\boldsymbol{x}}_{BG} \qquad \textbf{Eq. 13}$$

The uncertainty of these plume signal is the sum of the uncertainties of the satellite data $\boldsymbol{S}_{y,n}$ and the uncertainty of the estimated background:

$$\mathbf{S}_{\mathbf{y,plume}} \approx \cancel{=} \mathbf{S}_{y,n} + \mathbf{K}_{\mathbf{BG}} \cancel{\mathbf{K}} \mathbf{S}_{\hat{x}_{BG}} \mathbf{K}_{\mathbf{BG}} \cancel{\mathbf{K}}^{T} \qquad \textbf{Eq. 14}$$

It notes that Eq. 14 is an approximation, because the two error components are not completely independent ($\boldsymbol{S}_{y,BG}$ and thus $\mathbf{S}_{\hat{x}_{BG}}$ depend also on the noise of the observations, see description for calculating $\boldsymbol{S}_{y,BG}$ in the context of Eq. 11).

B.2 Fitting of CH_4 emission rates

Because the CH_4 plume signal is rather weak compared to the CH_4 background uncertainty and the noise level of the satellite data, we have to work with averages in order to reduce the data noise. The averaging is made by classifying the observation in two predominant wind categories. We calculate the average plume maps for the southwest and northeast wind situations (see Figure 6 and Figure 8). Then we calculate the difference between the south-west and north-east plume maps (the wind-assigned anomalies or Δ-maps). All the calculations are made by binning all observations that fall within a certain 0.135° × 0.1° (longitude × latitude) area. In order to significantly reduce the data noise, we only consider averages for the 0.135°× 0.1° areas based on at least 25 individual observations made under southwest wind conditions and 25 individual observations made under northeast wind conditions. The binning, the averaging, the wind-assigned Δ-maps calculations, and the data number filtering is achieved by operator **D,** and we can write:

$$\Delta \boldsymbol{y}_{plume} = \mathbf{D} \boldsymbol{y}_{plume} \qquad \textbf{Eq. 15}$$

and

$$\Delta \mathbf{S}_{\mathbf{y,plume}} = \mathbf{D} \mathbf{S}_{\mathbf{y,plume}} \mathbf{D}^{T} \qquad \textbf{Eq. 16}$$

Here $\boldsymbol{\Delta y_{plume}}$ is a column vector whose elements capture the different signal of the two wind directions at the different locations and $\boldsymbol{\Delta S_{\mathrm{y,plume}}}$ is the corresponding uncertainty covariance.

For modelling the plume signals we use a priori knowledge of CH_4 emission locations, i.e. assuming a repartition of the emissions between the three waste disposal sites according to Table 2 (see Sect. 3.1). Together with information from the wind, we then model the CH_4 plume's wind-assigned anomaly signal $\boldsymbol{\Delta y_{plume}}$:

$$\boldsymbol{\Delta y_{plume}} = \boldsymbol{\Delta k x} \qquad \textbf{Eq. 17}$$

Here the Jacobian $\boldsymbol{\Delta k}$ (a column vector) represents the wind-assigned anomaly model as described in Sect. 2.3. It describes how an emission at the waste disposal sites according to Table 2 would be seen in the difference signal. We are interested in the coefficient x (a scalar describing how the assumed emissions from Table 2 have to be scaled by a common factor in order to achieve the best agreement with the observed plume).

Similar to Eq. 9 and Eq. 10 we write:

$$\hat{x} = \boldsymbol{g}^T \boldsymbol{\Delta y_{plume}} \qquad \textbf{Eq. 18}$$

with the row vector

$$\boldsymbol{g}^T = \left(\boldsymbol{\Delta k^T} \boldsymbol{\Delta}\mathbf{S_{y,plume}}^{-1} \boldsymbol{\Delta k}\right)^{-1} \boldsymbol{\Delta k^T} \boldsymbol{\Delta}\mathbf{S_{y,plume}}^{-1} \qquad \textbf{Eq. 19}$$

This fitting of the emission rate correctly considers the respective uncertainty of the difference signals at the different locations.

Because of the small plume signals, it is important to estimate the reliability of the fitted emission rate. The uncertainty of x due to the background uncertainty and the noise in the satellite data can be estimated as:

$$\epsilon_{BG} = \sqrt{\boldsymbol{g}^T \mathbf{D} \cancel{\boldsymbol{K}} \mathbf{K_{BG}} \mathbf{S_{\hat{x},BG}} \cancel{\boldsymbol{K}} \mathbf{K_{BG}}^{\boldsymbol{T}} \mathbf{D^T} \boldsymbol{g}} \qquad \textbf{Eq. 20}$$

and

$$\epsilon_n = \sqrt{\boldsymbol{g}^T \mathbf{D} \mathbf{S_{y,n}} \mathbf{D^T} \boldsymbol{g}} \qquad \textbf{Eq. 21}$$

respectively. However, as aforementioned these two error components are not completely independent.

References

Alvarez, R. A., Zavala-Araiza, D., Lyon, D. R., Allen, D. T., Barkley, Z. R., Brandt, A. R., Davis, K. J., Herndon, S. C., Jacob, D. J., Karion, A., Kort, E. A., Lamb, B. K., Lauvaux, T., Maasakkers, J. D., Marchese, A. J., Omara, M., Pacala, S. W., Peischl, J., Robinson, A. L., Shepson, P. B., Sweeney, C., Townsend-Small, A., Wofsy, S. C. and Hamburg, S. P.: Assessment of methane emissions from the U.S. oil and gas supply chain, Science (80-.)., 361(6398), 186 LP – 188, doi:10.1126/science.aar7204, 2018.

Borsdorff, T., García Reynoso, A., Maldonado, G., Mar-Morales, B., Stremme, W., Grutter, M., and Landgraf, J.: Monitoring CO emissions of the metropolis Mexico City using TROPOMI CO observations, Atmos. Chem. Phys., 20, 15761–15774, https://doi.org/10.5194/acp-20-15761-2020, 2020.

Bousquet, P., Ciais, P., Miller, J. B., Dlugokencky, E. J., Hauglustaine, D. A., Prigent, C., Van der Werf, G. R., Peylin, P., Brunke, E.-G., Carouge, C., Langenfelds, R. L., Lathière, J., Papa, F., Ramonet, M., Schmidt, M., Steele, L. P., Tyler, S. C. and White, J.: Contribution of anthropogenic and natural sources to atmospheric methane variability, Nature, 443(7110), 439–443, doi:10.1038/nature05132, 2006.

Beirle, S., Boersma, K. F., Platt, U., Lawrence, M. G., and Wagner, T.: Megacity Emissions and Lifetimes of Nitrogen Oxides Probed from Space, Science, 333, 1737, https://doi.org/10.1126/science.1207824, 2011.

Briggs, G. A.: Diffusion estimation for small emissions. Preliminary report, Tech. Rep. TID-28289, National Oceanic and Atmospheric Administration, Oak Ridge, Tenn. (USA). Atmospheric Turbulence and Diffusion Lab., https://doi.org/10.2172/5118833, https://www.osti.gov/biblio/5118833-diffusion-estimation-small-emissions-preliminary-report, 1973.

Butz, A., Hasekamp, O. P., Frankenberg, C., and Aben, I.: Retrievals of atmospheric CO2 from simulated space-borne measurements of backscattered near-infrared sunlight: accounting for aerosol effects, Appl. Opt. 48, 3322-3336, 2009.

Butz, A., Guerlet, S., Hasekamp, O., Schepers, D., Galli, A., Aben, I., Frankenberg, C., Hartmann, J.-M., Tran, H., Kuze, A., Keppel-Aleks, G., Toon, G., Wunch, D., Wennberg, P., Deutscher, N., Griffith, D., Macatangay, R., Messerschmidt, J., Notholt, J., and Warneke, T.: Toward accurate CO2 and CH4 observations from GOSAT, Geophysical Research Letters, 38, https://doi.org/10.1029/2011GL047888, https://agupubs.onlinelibrary.wiley.com/doi/abs/10.1029/2011GL047888, 2011.

Butz, A., Galli, A., Hasekamp, O., Landgraf, J., Tol, P., and Aben, I.: TROPOMI aboard Sentinel-5 Precursor: Prospective performance of CH4 retrievals for aerosol and cirrus loaded atmospheres, Remote Sens. Environ., 120, 267–276, https://doi.org/10.1016/j.rse.2011.05.030, 2012.

Cambaliza, M. O. L., Shepson, P. B., Bogner, J., Caulton, D. R., Stirm, B., Sweeney, C., Montzka, S. A., Gurney, K. R., Spokas, K., Salmon, O. E., Lavoie, T. N., Hendricks, A., Mays, K., Turnbull, J., Miller, B. R., Lauvaux, T., Davis, K., Karion, A., Moser, B., Miller, C., Obermeyer, C., Whetstone, J., Prasad, K., Miles, N., and Richardson, S.: Quantification and source apportionment of the methane emission flux from the city of Indianapolis, Elementa: Science of the Anthropocene, 3, https://doi.org/10.12952/journal.elementa.000037, 2015.

Csanady, G. T.: Turbulent Diffusion in the Environment, Springer Netherlands, Dordrecht, https://doi.org/10.1007/978-94-010-2527-0, 1973.

Chen, J., Viatte, C., Hedelius, J. K., Jones, T., Franklin, J. E., Parker, H., Gottlieb, E. W., Wennberg, P. O., Dubey, M. K., and Wofsy, S. C.: Differential column measurements using compact solar-tracking spectrometers, Atmos. Chem. Phys., 16, 8479–8498, https://doi.org/10.5194/acp-16-8479-2016, 2016.

Chynoweth, D. P., Owens, J. M. and Legrand, R.: Renewable methane from anaerobic digestion of biomass, Renew. Energy, 22(1), 1–8, doi:https://doi.org/10.1016/S0960-1481(00)00019-7, 2001.

Clerbaux, C., Hadji-Lazaro, J., Turquety, S., Mégie, G., and Coheur, P.-F.: Trace gas measurements from infrared satellite for chemistry and climate applications, Atmos. Chem. Phys., 3, 1495–1508, https://doi.org/10.5194/acp-3-1495-2003, 2003.

Copernicus Climate Change Service (C3S): ERA5: Fifth generation of ECMWF atmospheric reanalyses of the global climate . Copernicus Climate Change Service Climate Data Store (CDS), date of access. https://cds.climate.copernicus.eu/cdsapp#!/home, 2017.

Crippa, M., Oreggioni, G., Guizzardi, D., Muntean, M., Schaaf, E., Lo Vullo, E., Solazzo, E., Monforti-Ferrario, F., Olivier, J. G. J., and Vignati, E.: Fossil CO2 and GHG emissions of all world countries – 2019 Report, EUR 29849 EN, Publications Office of the European Union, Luxembourg, JRC117610, https://doi.org/10.2760/687800, ISBN 978-92-76-11100-9, 2019.

De Gouw, J. A., Veefkind, J. P., Roosenbrand, E., Dix, B., Lin, J. C., Landgraf, J., and Levelt, P. F.: Daily Satellite Observations of Methane from Oil and Gas Production Regions in the United States, Scientific Reports, 10, 1379, https://doi.org/10.1038/s41598-020-57678-4, 2020.

De Wachter, E., Kumps, N., Vandaele, A. C., Langerock, B., and De Mazière, M.: Retrieval and validation of MetOp/IASI methane, Atmos. Meas. Tech., 10, 4623–4638, https://doi.org/10.5194/amt-10-4623-2017, 2017.

Delkash, M, Zhou, B., Han, B., Chow, F. K., Rella, C. W. and Imhoff, P. T.: Short-term landfill methane emissions dependency on wind, Waste Management, 55, 288-298, https://doi.org/10.1016/j.wasman.2016.02.009, 2016.

Dietrich, F., Chen, J., Voggenreiter, B., Aigner, P., Nachtigall, N., and Reger, B.: MUCCnet: Munich Urban Carbon Column network, Atmos. Meas. Tech., 14, 1111–1126, https://doi.org/10.5194/amt-14-1111-2021, 2021.

Dlugokencky, E. J., Nisbet, E. G., Fisher, R., and Lowry, D.: Global atmospheric methane: budget, changes and dangers, Philos. T. R. Soc. A, 369, 2058–2072, 2011.

Etminan, M., Myhre, G., Highwood, E. J., and Shine, K. P., Radiative forcing of carbon dioxide, methane, and nitrous oxide: A significant revision of the methane radiative forcing, Geophys. Res. Lett., 43, 12,614– 12,623, doi:10.1002/2016GL071930, 2016.

Farr, T. G., Rosen, P. A., Caro, E., Crippen, R., Duren, R., Hensley, S., Kobrick, M., Paller, M., Rodriguez, E., Roth, L., Seal, D., Shaffer, S., Shimada, J., Umland, J., Werner, M., Oskin, M., Burbank, D., and Alsdorf, D.: The Shuttle Radar Topography Mission, Reviews of Geophysics, 45, https://doi.org/10.1029/2005RG000183, 2007.

Frankenberg, C., Meirink, J. F., Bergamaschi, P., Goede, A. P. H., Heimann, M., Körner, S., Platt, U., van Weele, M., and Wagner, T.: Satellite chartography of atmospheric methane from SCIAMACHY on board ENVISAT: Analysis of the years 2003 and 2004, J. Geophys. Res., 111, D07303, doi:10.1029/2005JD006235, 2006.

Frey, M., Hase, F., Blumenstock, T., Groß, J., Kiel, M., Mengistu Tsidu, G., Schäfer, K., Sha, K. M., and Orphal, J.: Calibration and instrumental line shape characterization of a set of portable FTIR spectrometers for detecting greenhouse gas emissions, Atmos. Meas. Tech., 8, 3047–3057, doi:10.5194/amt-8-3047-2015, 2015.

Frey, M., Sha, M. K., Hase, F., Kiel, M., Blumenstock, T., Harig, R., Surawicz, G., Deutscher, N. M., Shiomi, K., Franklin, J. E., Bösch, H., Chen, J., Grutter, M., Ohyama, H., Sun, Y., Butz, A., Mengistu Tsidu, G., Ene, D., Wunch, D., Cao, Z., Garcia, O., Ramonet, M., Vogel, F., and Orphal, J.: Building the COllaborative Carbon Column Observing Network (COCCON): long-term stability and ensemble performance of the EM27/SUN Fourier transform spectrometer, Atmos. Meas. Tech., 12, 1513-1530, https://doi.org/10.5194/amt-12-1513-2019, 2019.

García, O. E., Schneider, M., Ertl, B., Sepúlveda, E., Borger, C., Diekmann, C., Wiegele, A., Hase, F., Barthlott, S., Blumenstock, T., Raffalski, U., Gómez-Peláez, A., Steinbacher, M., Ries, L., and de Frutos, A. M.: The MUSICA IASI CH4 and N2O products and their comparison to HIPPO, GAW and NDACC FTIR references, Atmos. Meas. Tech., 11, 4171–4215, https://doi.org/10.5194/amt-11-4171-2018, 2018.

García, O., J.-A. Morgui, R. Curcoll, C. Estruch, E. Sepúlveda, R. Ramos, E. Cuevas, Characterizing methane emissions in Madrid City within the MEGEI-MAD project: the temporal and spatial ground-based mobile approach, 8th International Symposium on Non-CO2 Greenhouse Gases (NCGG8), Amsterdam (The Netherlands), June 12-14, 2019.

García, O., E. Sepúlveda, J.-A. Morgui, M. Frey, C. Schneider, R. Curcoll, C. Estruch, R. Ramos, C. Torres, S.F. León-Luis, F. Hase, A. Butz, C. Toledano, E. Cuevas, T. Blumenstock, M. Guevara, O. Jorba, C. Pérez, J. J. Bustos, C. Marrero, J. López-Solano, P.-M. Romero-Campos, and V. Carreño, Monitoring of Greenhouse Gas Emissions in Madrid (MEGEI-MAD), in preparation, 2021.

Gifford, F. A.: Turbulent diffusion-typing schemes: a review, http://inis.iaea.org/Search/search.aspx?orig_q=RN:8296495, 1976.

Gisi, M., Hase, F., Dohe, S., Blumenstock, T., Simon, A., and Keens, A.: XCO2-measurements with a tabletop FTS using solar absorption spectroscopy, Atmos. Meas. Tech., 5, 2969–2980, doi:10.5194/amt-5-2969-2012, 2012.

Guerlet, S., Butz, A., Schepers, D., Basu, S., Hasekamp, O. P., Kuze, A., Yokota, T., Blavier, J.-F., Deutscher, N. M., Griffith, D. W. T., Hase, F., Kyro, E., Morino, I., Sherlock, V., Sussmann, R., Galli, A., Aben, I.: Impact of aerosol and thin cirrus on retrieving and validating XCO2 from GOSAT shortwave infrared measurements, J. Geophys. Res. Atmos., 118, 4887–4905, doi:10.1002/jgrd.50332, 2013.

Hakkarainen, J., Ialongo, I., Tamminen, J.: Direct space-based observations of anthropogenic CO2 emission areas from OCO-2. Geophys. Res. Lett., 43, 11400–11406, doi:10.1002/2016GL070885, 2016.

Hakkarainen, J., Ialongo, I., and Maksyutov, S.: Crisp, D. Analysis of Four Years of Global XCO2 Anomalies as Seen by Orbiting Carbon Observatory-2. Remote Sens., 11, 850, https://doi.org/10.3390/rs11070850, 2019.

Hase, F., Frey, M., Blumenstock, T., Groß, J., Kiel, M., Kohlhepp, R., Mengistu Tsidu, G., Schäfer, K., Sha, M. K., and Orphal, J.: Application of portable FTIR spectrometers for detecting greenhouse gas emissions of the major city Berlin, Atmos. Meas. Tech., 8, 3059–3068, https://doi.org/10.5194/amt-8-3059-2015, 2015.

Hase, F., Frey, M., Kiel, M., Blumenstock, T., Harig, R., Keens, A., and Orphal, J.: Addition of a channel for XCO observations to a portable FTIR spectrometer for greenhouse gas measurements, Atmos. Meas. Tech., 9, 2303–2313, https://doi.org/10.5194/amt-9-2303-2016, 2016.

Hasekamp, O. P., and Butz, A.: Efficient calculation of intensity and polarization spectra in vertically inhomogeneous scattering and absorbing atmospheres, J. Geophys. Res., 113, D20309, doi:10.1029/2008JD010379, 2008.

Hasekamp, O., Lorente, A., Hu, H., Butz, A., aan de Brugh, J., and Landgraf, J.: Algorithm Theoretical Baseline Document for Sentinel-5 Precursor methane retrieval, http://www.tropomi.eu/documents/atbd/, 2019.

Hu, H., Landgraf, J., Detmers, R., Borsdorff, T., Brugh, J. A. d., Aben, I., Butz, A., and Hasekamp, O.: Toward Global Mapping of Methane With TROPOMI: First Results and Intersatellite Comparison to GOSAT, Geophys. Res. Lett., 45, 3682–3689, https://doi.org/10.1002/2018GL077259, 2018.

Jacobs, N., Simpson, W. R., Wunch, D., O'Dell, C. W., Osterman, G. B., Hase, F., Blumenstock, T., Tu, Q., Frey, M., Dubey, M. K., Parker, H. A., Kivi, R., and Heikkinen, P.: Quality controls, bias, and seasonality of CO2 columns in the boreal forest with Orbiting Carbon Observatory-2, Total Carbon Column Observing Network, and EM27/SUN measurements, Atmos. Meas. Tech., 13, 5033–5063, https://doi.org/10.5194/amt-13-5033-2020, 2020.

Kenagy, H. S., Sparks, T. L., Ebben, C. J., Wooldrige, P. J., Lopez-Hilfiker, F. D., Lee, B. H., Thornton, J. A., McDuffie, E. E., Fibiger, D. L., Brown, S. S., Montzka, D. D., Weinheimer, A. J., Schroder, J. C., Campuzano-Jost, P., Day, D. A., Jimenez, J. L., Dibb, J. E., Campos, T., Shah, V., Jaeglé, L. and Cohen, R. C.: NOx Lifetime and NOy Partitioning During WINTER, J. Geophys. Res. Atmos., 123(17), 9813–9827, doi:https://doi.org/10.1029/2018JD028736, 2018.

Kirschke, S., Bousquet, P., Ciais, P., Saunois, M., Canadell, J., Dlugokencky, E., Bergamaschi, P., Bergmann, D., Blake, D., Bruhwiler, L., Cameron-Smith, P., Castaldi, S., Chevallier, F., Feng, L., Fraser, A., Heimann, M., Hodson, E., Houweling, S., Josse, B., Fraser, P., Krummel, P., Lamarque, J.-F., Langenfelds, R., Le Quere, C., Naik, V., O'Doherty, S., Palmer, P., Pison, I., Plummer, D., Poulter, B., Prinn, R., Rigby, M., Ringeval, B., Santini, M., Schmidt, M., Shindell, D., Simpson, I., Spahni, R., Steele, L., Strode, S., Sudo, K., Szopa, S., Van Der Werf, G., Voulgarakis, A., Van Weele, M., Weiss, R., Williams, J., and Zeng, G.: Three decades of global methane sources and sinks, Nat. Geosci., 6, 813–823, https://doi.org/10.1038/ngeo1955, 2013.

Klappenbach, F., Bertleff, M., Kostinek, J., Hase, F., Blumenstock, T., Agusti-Panareda, A., Razinger, M., and Butz, A.: Accurate mobile remote sensing of XCO2 and XCH4 latitudinal transects from aboard a research vessel, Atmos. Meas. Tech., 8, 5023–5038, doi:10.5194/amt-8-5023-2015, 2015.

Klausner, T., Mertens, M., Huntrieser, H., Galkowski, M., Kuhlmann, G., Baumann, R., Fiehn, A., Jöckel, P., Pühl, M., and Roiger, A.: Urban greenhouse gas emissions from the Berlin area: A case study using airborne CO2 and CH4 in situ observations in summer 2018, Elementa: Science of the Anthropocene, 8, https://doi.org/10.1525/elementa.411, 2020.

Kort, E. A., Frankenberg, C., Costigan, K. R., Lindenmaier, R., Dubey, M. K., and Wunch, D.: Four corners: The largest US methane anomaly viewed from space, Geophys. Res. Lett., 41, 6898–6903, 2014.

Kulawik, S. S., Worden, J. R., Payne, V. H., Fu, D., Wofsy, S. C., McKain, K., Sweeney, C., Daube Jr., B. C., Lipton, A., Polonsky, I., He, Y., Cady-Pereira, K. E., Dlugokencky, E. J., Jacob, D. J., and Yin, Y.: Evaluation of single-footprint AIRS CH4 profile retrieval uncertainties using aircraft profile measurements, Atmos. Meas. Tech., 14, 335–354, https://doi.org/10.5194/amt-14-335-2021, 2021.

Kuze, A., Suto, H., Nakajima, M., and Hamazaki, T.: Thermal and near infrared sensor for carbon observation Fourier-transform spectrometer on the Greenhouse Gases Observing Satellite for greenhouse gases monitoring, Appl. Opt., 48, 6716–6733, 2009.

Kuze, A., Kikuchi, N., Kataoka, F., Suto, H., Shiomi, K., and Kondo, Y.: Detection of Methane Emission from a Local Source Using GOSAT Target Observations. Remote Sens., 12, 267, 2020.

Landgraf, J., Butz, A., Hasekamp, O., Hu, H., and aan de Brugh, J.: Sentinel 5 L2 Prototype Processors, Algorithm Theoretical Baseline Document: Methane Retrieval, 2019.

Lorente, A., Borsdorff, T., Butz, A., Hasekamp, O., aan de Brugh, J., Schneider, A., Wu, L., Hase, F., Kivi, R., Wunch, D., Pollard, D. F., Shiomi, K., Deutscher, N. M., Velazco, V. A., Roehl, C. M., Wennberg, P. O., Warneke, T., and Landgraf, J.: Methane retrieved from TROPOMI: improvement of the data product and validation of the first 2 years of measurements, Atmos. Meas. Tech., 14, 665–684, https://doi.org/10.5194/amt-14-665-2021, 2021.

Luther, A., Kleinschek, R., Scheidweiler, L., Defratyka, S., Stanisavljevic, M., Forstmaier, A., Dandocsi, A., Wolff, S., Dubravica, D., Wildmann, N., Kostinek, J., Jöckel, P., Nickl, A.-L., Klausner, T., Hase, F., Frey, M., Chen, J., Dietrich, F., Nęcki, J., Swolkień, J., Fix, A., Roiger, A., and Butz, A.: Quantifying CH4 emissions from hard coal mines using mobile sun-viewing Fourier transform spectrometry, Atmos. Meas. Tech., 12, 5217–5230, https://doi.org/10.5194/amt-12-5217-2019, 2019.

Maasakkers, J. D., Jacob, D. J., Sulprizio, M. P., Scarpelli, T. R., Nesser, H., Sheng, J.-X., Zhang, Y., Hersher, M., Bloom, A. A., Bowman, K. W., Worden, J. R., Janssens-Maenhout, G., and Parker, R. J.: Global distribution of methane emissions, emission trends, and OH concentrations and trends inferred from an inversion of GOSAT satellite data for 2010–2015, Atmos. Chem. Phys., 19, 7859–7881, https://doi.org/10.5194/acp-19-7859-2019, 2019.

Marais, E. A., Jacob, D. J., Wecht, K., Lerot, C., Zhang, L., Yu, K., Kurosu, T. P., Chance, K., and Sauvage, B.: Anthropogenic emissions in Nigeria and implications for ozone air quality: a view from space, Atmos. Environ., 99, 32–40, 2014.

Masters, G. M.: Introduction to Environmental Engineering and Science, Prentice-Hall, Inc., 2nd edn., 1998.

Martin, D. O.: Comment on “The Change of Concentration Standard Deviations with Distance”, J. Air Pollut. Control Assoc., 26, 145–147, https://doi.org/10.1080/00022470.1976.10470238, 1976.

Pandey, S., Gautam, R., Houweling, S., van der Gon, H. D., Sadavarte, P., Borsdorff, T., Hasekamp, O., Landgraf, J., Tol, P., van Kempen, T., Hoogeveen, R., van Hees, R., Hamburg, S. P., Maasakkers, J. D., and Aben, I.: Satellite observations reveal extreme methane leakage from a natural gas well blowout, Proc Natl Acad Sci USA, 116, 26376, https://doi.org/10.1073/pnas.1908712116, 2019.

Pasquill, F.: THE METEOROLOGICAL MAGAZINE, Meteorol. Mag., 90, 33–49, https://doi.org/10.1175/1520-0493(1920)48<219e:tmm>2.0.co;2, 1961.

Rachor, I. M., Gebert, J., Gröngröft, A., Pfeiffer, E.-M.: Variability of methane emissions from an old landfill over different time-scales. Eur. J. Soil Sci. 64, 16–26, https://doi.org/10.1111/ejss.12004, 2013.

Saunois, M., Jackson, R. B., Bousquet, P., Poulter, B., and Canadell, J. G.: The growing role of methane in anthropogenic climate change, Environ. Res. Lett., 11, 120207, https://doi.org/10.1088/1748-9326/11/12/120207, 2016.

Saunois, M., Stavert, A. R., Poulter, B., Bousquet, P., Canadell, J. G., Jackson, R. B., Raymond, P. A., Dlugokencky, E. J., Houweling, S., Patra, P. K., Ciais, P., Arora, V. K., Bastviken, D., Bergamaschi, P., Blake, D. R., Brailsford, G., Bruhwiler, L., Carlson, K. M., Carrol, M., Castaldi, S., Chandra, N., Crevoisier, C., Crill, P. M., Covey, K., Curry, C. L., Etiope, G., Frankenberg, C., Gedney, N., Hegglin, M. I., Höglund-Isaksson, L., Hugelius, G., Ishizawa, M., Ito, A., Janssens-Maenhout, G., Jensen, K. M., Joos, F., Kleinen, T., Krummel, P. B., Langenfelds, R. L., Laruelle, G. G., Liu, L., Machida, T., Maksyutov, S., McDonald, K. C., McNorton, J., Miller, P. A., Melton, J. R., Morino, I., Müller, J., Murguia-Flores, F., Naik, V., Niwa, Y., Noce, S., O'Doherty, S., Parker, R. J., Peng, C., Peng, S., Peters, G. P., Prigent, C., Prinn, R., Ramonet, M., Regnier, P., Riley, W. J., Rosentreter, J. A., Segers, A., Simpson, I. J., Shi, H., Smith, S. J., Steele, L. P., Thornton, B. F., Tian, H., Tohjima, Y., Tubiello, F. N., Tsuruta, A., Viovy, N., Voulgarakis, A., Weber, T. S., van Weele, M., van der Werf, G. R., Weiss, R. F., Worthy, D., Wunch, D., Yin, Y., Yoshida, Y., Zhang, W., Zhang, Z., Zhao, Y., Zheng, B., Zhu, Q., Zhu, Q., and Zhuang, Q.: The Global Methane Budget 2000–2017, Earth Syst. Sci. Data, 12, 1561–1623, https://doi.org/10.5194/essd-12-1561-2020, 2020.

Sánchez, C., de la Fuente, M. del M., Narros, A., del Peso, I. and Rodríguez, E.: Comparison of modeling with empirical calculation of diffuse and fugitive methane emissions in a Spanish landfill, J. Air Waste Manage. Assoc., 69(3), 362–372, doi:10.1080/10962247.2018.1541029, 2019.

Siddans, R., Knappett, D., Kerridge, B., Waterfall, A., Hurley, J., Latter, B., Boesch, H., and Parker, R.: Global height-resolved methane retrievals from the Infrared Atmospheric Sounding Interferometer (IASI) on MetOp, Atmos. Meas. Tech., 10, 4135–4164, https://doi.org/10.5194/amt-10-4135-2017, 2017.

Schneider, M., Ertl, B., Diekmann, C. J., Khosrawi, F., Röhling, A. N., Hase, F., Dubravica, D., García, O. E., Sepúlveda, E., Borsdorff, T., Landgraf, J., Lorente, A., Chen, H., Kivi, R., Laemmel, T., Ramonet, M., Crevoisier, C., Pernin, J., Steinbacher, M., Meinhardt, F., Deutscher, N. M., Griffith, D. W. T., Velazco, V. A., and Pollard, D. F.: Synergetic use of IASI and TROPOMI space borne sensors for generating a tropospheric methane profile product, Atmos. Meas. Tech. Discuss. [preprint], https://doi.org/10.5194/amt-2021-31, in review, 2021a.

Schneider, M., Ertl, B., Diekmann, C. J., Khosrawi, F., Weber, A., Hase, F., Höpfner, M., García, O. E., Sepúlveda, E., and Kinnison, D.: Design and description of the MUSICA IASI full retrieval product, Earth Syst. Sci. Data Discuss. [preprint], https://doi.org/10.5194/essd-2021-75, in review, 2021b.

Schneider, M., Ertl, B., Diekmann, C.: MUSICA IASI full retrieval product standard output (processing version 3.2.1). Institute of Meteorology and Climate Reasearch, Atmospheric Trace Gases and Remote Sensing (IMK-ASF), Karlsruhe Institute of Technology (KIT). DOI: 10.35097/408, 2021c.

Schneising, O., Burrows, J. P., Dickerson, R. R., Buchwitz, M., Reuter, M., and Bovensmann, H.: Remote sensing of fugitive methane emissions from oil and gas production in North American tight geologic formations, Earth's Future, 2, 548–558, 2014.

Schneising, O., Buchwitz, M., Reuter, M., Bovensmann, H., Burrows, J. P., Borsdorff, T., Deutscher, N. M., Feist, D. G., Griffith, D. W. T., Hase, F., Hermans, C., Iraci, L. T., Kivi, R., Landgraf, J., Morino, I., Notholt, J., Petri, C., Pollard, D. F., Roche, S., Shiomi, K., Strong, K., Sussmann, R., Velazco, V. A., Warneke, T., and Wunch, D.: A scientific algorithm to simultaneously retrieve carbon monoxide and methane from TROPOMI onboard Sentinel-5 Precursor, Atmos. Meas. Tech., 12, 6771–6802, https://doi.org/10.5194/amt-12-6771-2019, 2019.

Schneising, O., Buchwitz, M., Reuter, M., Vanselow, S., Bovensmann, H., and Burrows, J. P.: Remote sensing of methane leakage from natural gas and petroleum systems revisited, Atmos. Chem. Phys., 20, 9169–9182, https://doi.org/10.5194/acp-20-9169-2020, 2020.

Sha, M. K., De Mazière, M., Notholt, J., Blumenstock, T., Chen, H., Dehn, A., Griffith, D. W. T., Hase, F., Heikkinen, P., Hermans, C., Hoffmann, A., Huebner, M., Jones, N., Kivi, R., Langerock, B., Petri, C., Scolas, F., Tu, Q., and Weidmann, D.: Intercomparison of low and high resolution infrared spectrometers for ground-based solar remote sensing measurements of total column concentrations of CO2, CH4 and CO, Atmos. Meas. Tech. Discuss., https://doi.org/10.5194/amt-2019-371, in review, 2019.

Shah, V., Jacob, D. J., Li, K., Silvern, R. F., Zhai, S., Liu, M., Lin, J., and Zhang, Q.: Effect of changing NOx lifetime on the seasonality and long-term trends of satellite-observed tropospheric NO2 columns over China, Atmos. Chem. Phys., 20, 1483–1495, https://doi.org/10.5194/acp-20-1483-2020, 2020.

Smith, M. E.: Recommended guide for the prediction of the dispersion of airborne effluent, ASME, 1973.

Solazzo, E., Crippa, M., Guizzardi, D., Muntean, M., Choulga, M., and Janssens-Maenhout, G.: Uncertainties in the Emissions Database for Global Atmospheric Research (EDGAR) emission inventory of greenhouse gases, Atmos. Chem. Phys., 21, 5655–5683, https://doi.org/10.5194/acp-21-5655-2021, 2021.

Tu, Q., Hase, F., Blumenstock, T., Kivi, R., Heikkinen, P., Sha, M. K., Raffalski, U., Landgraf, J., Lorente, A., Borsdorff, T., Chen, H., Dietrich, F., and Chen, J.: Intercomparison of atmospheric CO2 and CH4 abundances on regional scales in boreal areas using Copernicus Atmosphere Monitoring Service (CAMS) analysis, COllaborative Carbon Column Observing Network (COCCON) spectrometers, and Sentinel-5 Precursor satellite observations, Atmos. Meas. Tech., 13, 4751–4771, https://doi.org/10.5194/amt-13-4751-2020, 2020a.

Tu, Q., Hase, F., Blumenstock, T., Schneider, M., Schneider, A., Kivi, R., Heikkinen, P., Ertl, B., Diekmann, C., Khosrawi, F., Sommer, M., Borsdorff, T., and Raffalski, U.: Intercomparison of arctic XH2O observations from three ground-based

Fourier transform infrared networks and application for satellite validation, Atmos. Meas. Tech., 14, 1993–2011, https://doi.org/10.5194/amt-14-1993-2021, 2021b.

Tunnicliffe, R. L., Ganesan, A. L., Parker, R. J., Boesch, H., Gedney, N., Poulter, B., Zhang, Z., Lavrič, J. V., Walter, D., Rigby, M., Henne, S., Young, D., and O'Doherty, S.: Quantifying sources of Brazil's CH4 emissions between 2010 and 2018 from satellite data, Atmos. Chem. Phys., 20, 13041–13067, https://doi.org/10.5194/acp-20-13041-2020, 2020.

Turner, A. J., Jacob, D. J., Wecht, K. J., Maasakkers, J. D., Lundgren, E., Andrews, A. E., Biraud, S. C., Boesch, H., Bowman, K. W., Deutscher, N. M., Dubey, M. K., Griffith, D. W. T., Hase, F., Kuze, A., Notholt, J., Ohyama, H., Parker, R., Payne, V. H., Sussmann, R., Sweeney, C., Velazco, V. A., Warneke, T., Wennberg, P. O., and Wunch, D.: Estimating global and North American methane emissions with high spatial resolution using GOSAT satellite data, Atmos. Chem. Phys., 15, 7049–7069, https://doi.org/10.5194/acp-15-7049-2015, 2015.

Varon, D. J., McKeever, J., Jervis, D., Maasakkers, J. D., Pandey, S., Houweling, S., Aben, I., Scarpelli, T. and Jacob, D. J. : Satellite discovery of anomalously large methane point sources from oil/gas production, Geophysical Research Letters, 46, 13507– 13516. https://doi.org/10.1029/2019GL083798, 2019.

Varon, D. J., Jacob, D. J., Jervis, D. and McKeever, J.: Quantifying Time-Averaged Methane Emissions from Individual Coal Mine Vents with GHGSat-D Satellite Observations, Environ. Sci. Technol., 54(16), 10246–10253, doi:10.1021/acs.est.0c01213, 2020.

Veefkind, J., Aben, I., McMullan, K., örster, H., de Vries, J., Otter, G., Claas, J., Eskes, H., de Haan, J., Kleipool, Q., vanWeele, M., Hasekamp, O., Hoogeveen, R., Landgraf, J., Snel, R., Tol, P., Ingmann, P., P., V., Kruizinga, P., Vink, R., Visser, H., and Levelt, P.: TROPOMI on the ESA Sentinel-5 Precursor: A GMES mission for global observations of the atmospheric composition for climate, air quality and ozone layer applications, Remote Sens. Environ., 120, 70–83, doi:10.1016/j.rse.2011.09.027, 2012.

Vogel, F., Frey, M., Staufer, J., Hase, F., Broquet, G., Xueref-Remy, I., Chevallier, F., Ciais, P., Sha, M.K., Chelin, P., Jeseck, P., Janssen, C., Te, Y., Groß, J., Blumenstock, T., Tu, Q., Orphal, J.: XCO2 in an emission hot- spot region: the COCCON Paris campaign 2015, Atmospheric Chemistry and Physics, doi: 10.5194/acp-19-3271-2019, 2019.

Washenfelder, R. A., Toon, G. C., Blavier, J.-F., Yang, Z., Allen, N. T., Wennberg, P. O., Vay, S. A., Matross, D. M., and Daube, B. C. (2006), Carbon dioxide column abundances at the Wisconsin Tall Tower site, J. Geophys. Res., 111, D22305, doi:10.1029/2006JD007154, 2006.

World Meteorological Organization, 2020: WMO Greenhouse Gases Bulletin: The State of Greenhouse Gases in the Atmosphere Based on Global Observations through 2019. No. 16, available at: https://reliefweb.int/sites/reliefweb.int/files/resources/GHG-Bulletin-16_en.pdf, last access: 10 January 2020, 2019.

Wunch, D., Toon, G. C., Blavier, J.-F. L., Washenfelder, R. A., Notholt, J., Connor, B. J., Griffith, D. W. T., Sherlock, V., and Wennberg, P. O.: The total carbon column observing network, Philos. T. R. Soc. A, 369, 2087–2112, doi:10.1098/rsta.2010.0240, 2011.